

Supercluster A2142 and collapse in action - infalling and merging groups and galaxy transformations

Maret Einasto¹, Mirt Gramann¹, Changbom Park², Juhan Kim³, Boris Deshev^{1,4}, Elmo Tempel^{1,5}, Pekka Heinämäki⁶, Heidi Lietzen¹, Anne Lähteenmäki^{7,8}, Jaan Einasto^{1,9,10}, and Enn Saar^{1,9}

¹ Tartu Observatory, University of Tartu, Observatooriumi 1, 61602 Tõravere, Estonia

² School of Physics, Korea Institute for Advanced Study, 85 Hoegiro, Dong-Dae-Mun-Gu, Seoul 02455, Korea

³ Center for Advanced Computation, Korea Institute for Advanced Study, Hoegiro 87, Dong-dae-mun-gu, Seoul, 130-722, Korea

⁴ Institute of Physics, University of Tartu, W. Ostwaldi 1, 50411, Tartu, Estonia

⁵ Leibniz-Institut für Astrophysik Potsdam (AIP), An der Sternwarte 16, D-14482 Potsdam, Germany

⁶ Tuorla Observatory, University of Turku, Väisäläntie 20, Piikkiö, Finland

⁷ Aalto University, Metsähovi Radio Observatory, Metsähovintie 114, FI-02540 Kylmäla, Finland

⁸ Aalto University Department of Electronics and Nanoengineering, P.O. Box 15500, FI-00076 Aalto, Finland

⁹ Estonian Academy of Sciences, Kohtu 6, 10130 Tallinn, Estonia

¹⁰ ICRA Net, Piazza della Repubblica 10, 65122 Pescara, Italy

Received / Accepted

ABSTRACT

Context. Superclusters with collapsing cores represent dynamically evolving environments for galaxies, galaxy groups, and clusters. **Aims.** We study the dynamical state and properties of galaxies and groups in the supercluster SCI A2142 that has a collapsing core, to understand its possible formation and evolution.

Methods. We find the substructure of galaxy groups using normal mixture modelling. We have used the projected phase space (PPS) diagram, spherical collapse model, clustercentric distances, and magnitude gap between the brightest galaxies in groups to study the dynamical state of groups and to analyse group and galaxy properties. We compared the alignments of groups and their brightest galaxies with the supercluster axis.

Results. The supercluster core has a radius of about $8 h^{-1}$ Mpc and total mass $M_{\text{tot}} \approx 2.3 \times 10^{15} h^{-1} M_{\odot}$ and is collapsing. Galaxies in groups on the supercluster axis have older stellar populations than off-axis groups, with median stellar ages 4 – 6 and < 4 Gyr, correspondingly. The cluster A2142 and the group Gr8 both host galaxies with the oldest stellar populations among groups in SCI A2142 having the median stellar age $t > 8$ Gyr. Recently quenched galaxies and active galactic nuclei (AGNs) are mostly located at virial radii or in merging regions of groups, and at clustercentric distances $D_c \approx 6 h^{-1}$ Mpc. The most elongated groups lie along the supercluster axis and are aligned with it. Magnitude gaps between the brightest galaxies of groups are less than one magnitude, suggesting that groups in SCI A2142 are dynamically young.

Conclusions. The collapsing core of the supercluster, infall of galaxies and groups, and possible merging groups, which affect galaxy properties and may trigger the activity of AGNs, show how the whole supercluster is evolving.

Key words. large-scale structure of the Universe - galaxies: groups: general - galaxies: clusters: general

1. Introduction

The formation of the cosmic web of galaxies, galaxy groups, clusters, and superclusters connected by galaxy filaments started from the tiny density perturbations in a very early Universe (Jöeveer et al. 1978; Kofman & Shandarin 1988). The studies of protoclusters, progenitors of the present-day galaxy clusters, have shown that they start to form in regions of the highest density in the cosmic density field and are present already at redshifts $z \approx 6$ (Toshikawa et al. 2016; Overzier 2016; Lovell et al. 2018, and references therein). Galaxy protoclusters are the first sights of galaxy formation in a high redshift Universe (Chiang et al. 2017; Marrone et al. 2018; Pavese et al. 2018). Rich galaxy clusters grow through merging and accretion of smaller structures (galaxies and groups of galaxies) along filaments (Bond et al. 1996; van de Weygaert & Schaap 2009; Suhhonenko et al. 2011; Kravtsov & Borgani 2012;

Cautun et al. 2014, and references therein). Simulations show that the present-day rich galaxy clusters have assembled half of their mass since redshift $z \approx 0.5$, and they continue to grow (Wu et al. 2013; Chiang et al. 2013; Kim et al. 2015; Haines et al. 2015; Deshev et al. 2017; Einasto et al. 2018).

In the cosmic web the most luminous galaxy clusters are typically located in the high-density core regions of rich superclusters (Jöeveer & Einasto 1978; Jöeveer et al. 1978). The high-density cores of rich superclusters are the largest objects that may collapse now or during future evolution (Small et al. 1998; Reisenegger et al. 2000; Proust et al. 2006; Pearson et al. 2014; Gramann et al. 2015; O’Mill et al. 2015; Chon et al. 2015; Einasto et al. 2016). These cores form an evolving environment for the study of the formation, evolution and present-day properties of galaxies, groups, and clusters inside them.

In this paper we study the dynamical state and properties of galaxies and galaxy groups in the supercluster SCI A2142 embedding the very rich galaxy cluster A2142 (Einasto et al. 2015). The core of this supercluster is already collapsing (Einasto et al.

Send offprint requests to: Einasto, M.

2015; Gramann et al. 2015). In the collapsing cores of superclusters we can study various processes in groups and clusters which are responsible for transformation of galaxies from mostly blue, star-forming field galaxies to red, quiescent cluster population (see Haines et al. 2015; Rhee et al. 2017, for a review and references). Einasto et al. (2018) studied the properties of the most massive cluster in this supercluster, A2142. In this paper we extend this analysis to the whole supercluster. The main goal of this paper is to study the structure and galaxy content of the supercluster SCI A2142, and in this way to understand its possible formation and evolution. We have analysed whether the supercluster environment and infall of galaxies and groups into the main cluster of the supercluster, A2142, affects their properties. We find substructure of galaxy groups using normal mixture modelling, and apply the projected phase space (PPS) diagram, the spherical collapse model, a magnitude gap between the brightest galaxies in groups, and clustercentric distances to study the dynamical state of galaxy groups in the supercluster and analyse galaxy properties at various clustercentric distances. We have compared alignments of groups and their brightest galaxies, and the supercluster axis. We assumed the standard cosmological parameters: the Hubble parameter $H_0 = 100 h \text{ km s}^{-1} \text{ Mpc}^{-1}$, matter density $\Omega_m = 0.27$, and dark energy density $\Omega_\Lambda = 0.73$ (Komatsu et al. 2011).

2. Data

2.1. Supercluster, group, and filament data

Our galaxy, group, and supercluster data are based on the MAIN sample of the tenth data release of the Sloan Digital Sky Survey (SDSS, Aihara et al. 2011; Ahn et al. 2014). We used a spectroscopic galaxy sample with the apparent Galactic extinction corrected r magnitudes $r \leq 17.77$ and redshifts $0.009 \leq z \leq 0.200$. We corrected the redshifts of galaxies for the motion relative to the cosmic microwave background and computed the comoving distances of galaxies (Martínez & Saar 2002). Galaxies with unreliable parameters (large galaxies, which may have multiple entries in the sample, bright over-saturated stars that are classified as galaxies, and so on) were removed from the sample as described in detail in Tempel et al. (2012, 2014b).

The SDSS MAIN dataset was used to calculate the luminosity-density field to detect superclusters of galaxies as connected high-density volumes, to find groups of galaxies with the friends-of-friends algorithm, and to determine galaxy filaments by applying the Bisous process to the distribution of galaxies (Tempel et al. 2014a, 2016b). The data from supercluster, group, and filament catalogues were then used to select galaxy, group, and filament information for the supercluster SCI A2142. As in Einasto et al. (2015), galaxies are considered as members of filaments if their distance from the filament axis is up to $0.8 h^{-1} \text{ Mpc}$.

The galaxy luminosity density field was calculated using B_3 spline kernel with the smoothing length $8 h^{-1} \text{ Mpc}$:

$$B_3(x) = \frac{1}{12} (|x-2|^3 - 4|x-1|^3 + 6|x|^3 - 4|x+1|^3 + |x+2|^3). \quad (1)$$

We created a set of density contours by choosing a density threshold and defined connected volumes above a certain density threshold as superclusters. In order to choose the proper density level for determining individual superclusters, we analysed the properties of the density field superclusters at a series

of density levels. As a result we used the density level $D_8 = 5.0$ (in units of mean density, $\ell_{\text{mean}} = 1.65 \cdot 10^{-2} \frac{10^{10} h^{-2} L_\odot}{(h^{-1} \text{ Mpc})^3}$) to determine individual superclusters. At this density level superclusters in the richest chains of superclusters in the volume under study still form separate systems. At lower density levels they join into huge percolating systems. The calculation of the luminosity density field and determination of superclusters is described in detail in Liivamägi et al. (2012).

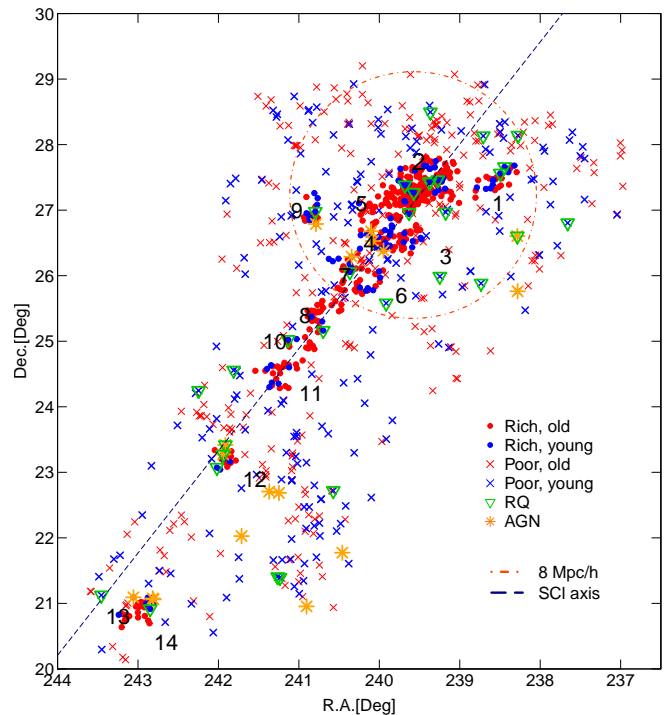


Fig. 1. Sky distribution of galaxies in SCI A2142. The red symbols show galaxies with old stellar populations ($D_n(4000) \geq 1.55$), and the blue symbols denote galaxies with young stellar populations ($D_n(4000) < 1.55$). Filled circles denote galaxies in rich groups with at least ten member galaxies. The crosses denote galaxies in poor groups with less than ten galaxies. The green triangles show recently quenched galaxies (RQ) with $D_n(4000) \leq 1.55$ and star formation rate $\log \text{SFR} < -0.5$. Orange stars indicate the positions of AGNs (see text for definitions). The red-orange circle shows a projected radius of about $8 h^{-1} \text{ Mpc}$. The dashed line shows the supercluster axis.

Supercluster catalogue and supercluster SCI A2142. Data on SCI A2142 are taken from the catalogue of galaxy superclusters by Liivamägi et al. (2012), in which SCI A2142 at redshift $z \approx 0.09$ has over a thousand member galaxies within the SDSS MAIN sample. The total length of this supercluster, defined as the maximum distance between galaxy pairs in the supercluster, is $\approx 50 h^{-1} \text{ Mpc}$ (Liivamägi et al. 2012). This supercluster was recently described in Einasto et al. (2015) and Gramann et al. (2015). They showed that SCI 2142 has a collapsing high-density core in an almost spherical main body with a radius of about $11 h^{-1} \text{ Mpc}$, and an almost straight tail. We used this definition for the main body and tail of the supercluster also in this paper.

Galaxy groups in the supercluster SCI A2142. We selected galaxy groups in SCI A2142 from the group catalogue by Tempel et al. (2014b), where galaxy groups were determined using the friends-of-friends (FoF) cluster analysis method introduced in cosmology by Zeldovich et al. (1982) and Huchra & Geller (1982). A galaxy belongs to a group of galaxies if this galaxy has at least one group member galaxy closer than

a linking length. In a flux-limited sample the density of galaxies slowly decreases with distance. To take this selection effect into account properly when constructing a group catalogue from a flux-limited sample, the linking length was rescaled with distance, calibrating the scaling relation by observed groups. As a result, the maximum sizes in the sky projection and the velocity dispersions of Tempel et al. (2014b) groups are similar at all distances. Details of the data reduction, group finding procedure, and description of the group catalogue can be found in Tempel et al. (2014b).

It is possible that our group finding algorithm combines together close groups, especially in high density regions of supercluster cores. Also, it may sometimes split or fragment single groups into several smaller groups (fragmentation of groups, see Duarte & Mamon 2015). Various group finding algorithms and mass estimation methods were compared and tested on mock galaxy catalogues in Old et al. (2014, 2015, 2018); Wojtak et al. (2018). This comparison showed that the method used in Tempel et al. (2014b) finds groups reasonably well. However, some individual groups may be combined or split erroneously. Below we discuss some such cases.

The supercluster SCI A2142 embeds 14 rich galaxy groups with at least ten member galaxies, nine of them in the main body of the supercluster at distances from the supercluster centre up to $11 h^{-1}$ Mpc, and five in the tail. The supercluster also has poor groups with less than ten galaxies, hosting in total 460 galaxies. We consider single galaxies as the brightest galaxies of faint groups in which other group members are fainter than the SDSS survey limit (Tempel et al. 2009). Data for the groups with at least ten member galaxies are given in Table 1. Masses of groups in Table 1 were calculated applying the virial theorem and assuming symmetry of galaxy velocity distribution, and the Navarro-Frenk-White (NFW) density profile for galaxy distribution in the plane of the sky. For a detailed description of how the masses and virial radii of groups were calculated, we refer to Tempel et al. (2014b).

The SDSS spectroscopic sample is incomplete because of fibre collisions. The smallest separation between spectroscopic fibres is $55''$, and approximately 6% of the potential targets for spectroscopy are without observed spectra because of this. We find that in our sample 55 galaxies have a neighbour without measured redshifts due to fibre collisions. We analysed the regions around these galaxies with radius of $55''$, and searched for galaxies possibly missing from our sample. We looked for objects in SDSS database classified as galaxies with apparent r magnitudes $r \leq 17.77$ and photometric redshifts in the same interval as galaxy or group to which they could belong (within error limits). In this way we have found 31 possible missing member galaxies of the SCI A2142, 18 of them in the main body of the supercluster. The number of such galaxies was the highest in Gr3 from which seven galaxies may be missing due to fibre collisions. We used photometric magnitudes of these galaxies when calculating median colour indexes of groups below.

Absolute magnitudes of galaxies are computed according to the formula

$$M_r = m_r - 25 - 5 \log_{10}(d_L) - K, \quad (2)$$

where d_L is the luminosity distance in units of h^{-1} Mpc and K is the $k+e$ -correction. The k -corrections were calculated with the KCORRECT(v4_2) code (Blanton & Roweis 2007) and the evolution corrections have been calibrated according to Blanton et al. (2003). Details about how the k and e -corrections were applied can be found in Tempel et al. (2014b). Tempel et al. (2014b) used slightly smaller evolution corrections

than Blanton et al. (2003). The value of $M_{\odot} = 4.53$ mag (in r -filter).

At the distance of SCI A2142, $\approx 265 h^{-1}$ Mpc, the galaxy sample is complete at the absolute magnitude limit $M_r = -19.6$ in units of $\text{mag} + 5 \log_{10} h$. In our study we used the full dataset of SCI A2142 to study the group content of the supercluster. For comparison of galaxy populations in different groups we used a magnitude-limited complete sample, excluding galaxies fainter than the completeness limit, $M_r = -19.6$ mag.

2.2. Galaxy populations

We obtained data on galaxy properties from the SDSS DR10 web page¹. Galaxy magnitudes and Petrosian radii were taken from the SDSS photometric data. We calculated galaxy colours as $(g-r)_0 = M_g - M_r$. The value $(g-r)_0 = 0.7$ is used to separate red and blue galaxies, where red galaxies have $(g-r)_0 \geq 0.7$. All magnitudes and colours correspond to the rest frame at redshift $z = 0$.

Galaxy stellar masses (M^*), star formation rates (SFRs), and $D_n(4000)$ index of galaxies are from the MPA-JHU spectroscopic catalogue (Tremonti et al. 2004; Brinchmann et al. 2004), from which the various properties of galaxies were obtained by fitting SDSS photometry and spectra with the stellar population synthesis models developed by Bruzual & Charlot (2003). The stellar masses of galaxies were derived as described by Kauffmann et al. (2003a). The SFRs were computed using the photometry and emission lines as described by Brinchmann et al. (2004) and Salim et al. (2007). The strength of the $D_n(4000)$ break (the ratio of the average flux densities in the band $4000 - 4100\text{\AA}$ and $3850 - 3950\text{\AA}$; $D_n(4000)$ index) is correlated with the time passed from the most recent star formation event and is defined as in Balogh et al. (1999). The $D_n(4000)$ index characterises star formation histories of galaxies and can be understood as an indicator for luminosity-weighted age.

The $D_n(4000)$ index was used to separate quiescent and star-forming galaxies. The higher the value of the $D_n(4000)$ index, the older are stellar populations in a galaxy. We applied values for quiescent galaxies with old stellar populations as having $D_n(4000) \geq 1.55$, 70% of all galaxies (73% in the main body and 63% in the tail). Star-forming galaxies with young stellar populations have $D_n(4000) < 1.55$. This limit was also used by Kauffmann et al. (2003b) and Haines et al. (2017) to separate young and old galaxies in the SDSS survey.

Stellar ages are from the Portsmouth group (Maraston et al. 2009). We divided galaxies into old and young stellar populations by stellar age using the age limit $t = 3$ Gyr. We found that 61% of galaxies in the supercluster have old stellar populations with stellar ages $t \geq 3$ Gyr (in supercluster main body 63%, and in the tail 56%). The $\log \text{SFR} \leq -0.5$ corresponds to quiescent galaxies (88% of galaxies). Actively star-forming galaxies are characterised by $\log \text{SFR} > -0.5$; this limit was also applied in Einasto et al. (2014).

Some star-forming galaxies have red colours and are known as red star-forming galaxies. Also, there are galaxies with low SFRs but also low values of $D_n(4000)$ index, which suggest that they may be recently quenched. We define recently quenched galaxies as those with $D_n(4000) \leq 1.55$ and $\log \text{SFR} < -0.5$ (31 galaxies, 0.03% of all galaxies). Red, high SFR galaxies are defined as galaxies with $g-r \geq 0.7$ and $\log \text{SFR} \geq -0.5$ (138 galaxies, 13% of galaxies).

¹ <http://skyserver.sdss3.org/dr10/en/help/browser/browser.aspx>

Table 1. Data on rich groups in the A2142 supercluster with at least ten member galaxies.

(1)	(2)	(3)	(4)	(5)	(6)	(7)	(8)	(9)	(10)	(11)
No.	ID	N_{gal}	R.A.	Dec.	Dist.	D_C	R_{vir}	L_{tot}	M_{dyn}	D_8
			[deg]	[deg]	[h^{-1} Mpc]	[h^{-1} Mpc]	[h^{-1} Mpc]	[$10^{10}h^{-2}L_{\odot}$]	[$10^{12}h^{-1}M_{\odot}$]	
Main body										
1	10570	27 (31)	238.53	27.47	268.6	4.4	0.53	51.3	60	13.7
2	3070	212	239.52	27.32	264.6	0.0	0.88	382.0	907	20.7
3	4952	54 (61)	239.78	26.56	260.1	3.3	0.70	111.0	214	17.1
4	32074	11	240.11	26.71	262.4	3.3	0.28	15.7	60	19.9
5	35107	10	240.13	27.01	258.7	2.4	0.47	13.9	30	14.2
6	14960	27 (30)	240.20	25.87	263.6	7.0	0.59	46.6	148	15.3
7	17779	20	240.38	26.16	261.1	6.0	0.40	35.1	104	16.4
8	6885	32	240.75	25.40	258.9	9.7	0.46	70.5	164	11.4
9	21183	21	240.83	26.95	265.0	5.4	0.34	36.5	61	15.2
Tail										
10	20324	11 (12)	240.95	24.95	259.7	12.0	0.45	17.4	78	10.4
11	10818	28 (32)	241.23	24.52	259.6	14.1	0.53	51.3	105	9.3
12	14283	19 (25)	241.90	23.21	260.3	20.9	0.40	34.4	65	7.3
13	10224	32	242.91	21.02	254.6	32.0	0.32	60.4	233	6.0
14	26895	12	243.08	20.77	254.8	33.2	0.41	16.5	49	5.9

Notes. Columns are as follows: (1): Order number of the group; (2): ID of the group from Tempel et al. (2014b) (Gr 3070 correspond to the Abell cluster A2142); (3): Number of galaxies in the group, N_{gal} . In parenthesis we give the total number of galaxies in a group, which takes into account also galaxies possibly missing from the group because of fibre collisions; (4)–(5): Group centre right ascension and declination; (6): Group centre comoving distance; (7): Group distance from the centre of the cluster A2142 (for brevity, clustercentric distance); (8): Group virial radius; (9): Group total luminosity; (10): Dynamical mass of the group assuming the NFW density profile, M_{dyn} ; (11): Luminosity-density field at the location of the group, D_8 , in units of the mean density as described in the text.

To identify galaxies with active nuclei (AGNs) we used the spectral classification by Brinchmann et al. (2004) based on emission-line ratios $[\text{O III}]/\text{H}\beta$ and $[\text{N II}]/\text{H}\alpha$. We find that SCI A2142 embeds 17 AGNs. According to the VLA FIRST survey data at 1.4 GHz² three of them are very low flux radio sources. We also identify FR II radio galaxy (J155852.66+262618.9) in the group Gr3 using the catalogue of FR II radio galaxies by Capetti et al. (2017).

We show the sky distribution of galaxies in the supercluster in Fig. 1. Figure 1 shows that most rich groups in the supercluster main body lie along the supercluster axis (on-axis groups). Only groups Gr1 and Gr9 lie farther away from the axis (off-axis groups), we call them according to their order number from Table 1). For details about SCI 2142 we refer to Einasto et al. (2015, 2018).

To characterise galaxies with different stellar populations we plot in Fig. 2 $D_n(4000)$ index versus stellar mass of galaxies in the supercluster. The colour-magnitude diagram for SCI A2142 is shown in Fig. 3. We plot galaxies with old and young stellar populations, recently quenched galaxies, and red, star-forming galaxies with different symbols. Here we also show the completeness limit in luminosity, $M_r = -19.6 + 5 \log_{10} h$ mag.

3. Methods

3.1. Dynamical state of groups: phase space diagram

The PPS diagram shows line-of-sight velocities of galaxies with respect to the cluster mean velocity (velocity offset) versus projected clustercentric distance. In this paper clustercentric distance D_C is defined as the projected distance from the centre of the cluster A2142 (actually superclustercentric distance; we use

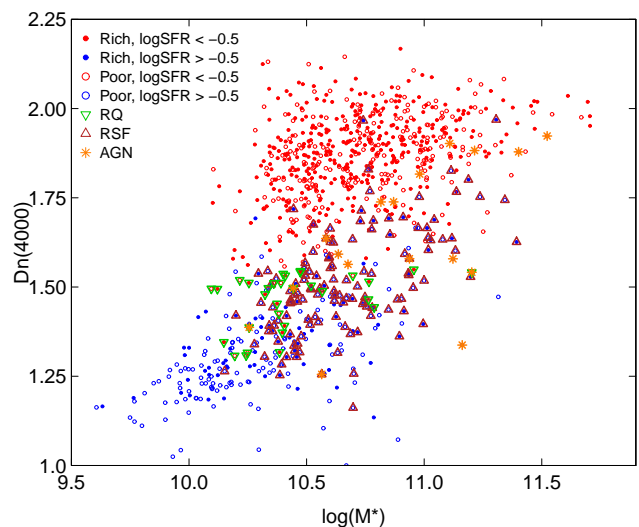


Fig. 2. $D_n(4000)$ index vs. stellar mass for SCI A2142. Red circles indicate low star formation rate galaxies with $\log \text{SFR} < -0.5$, and blue circles show high star formation rate galaxies with $\log \text{SFR} \geq -0.5$. Filled circles correspond to rich groups with $N_{\text{gal}} \geq 10$, and empty circles show galaxies in poor groups with $N_{\text{gal}} < 10$. The red triangles indicate red, high SFR galaxies defined as $g - r \geq 0.7$, and $\log \text{SFR} \geq -0.5$. Other notations are as in Fig. 1.

the term clustercentric distance for brevity). In the phase space diagram galaxies with different accretion histories populate different areas (Oman et al. 2013; Muzzin et al. 2014; Haines et al. 2015; Jaffé et al. 2015; Agulli et al. 2017; Paccagnella et al. 2017; Yoon et al. 2017; Rhee et al. 2017). Galaxies with early infall times (infall at redshifts $z > 1$) are located at small clustercentric distances in the virialised region. Recently infallen or still

² <http://sundog.stsci.edu/>.

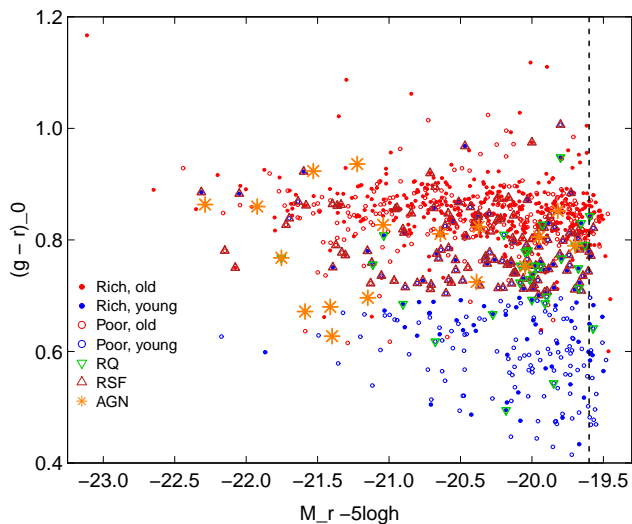


Fig. 3. Colour-magnitude diagram $(g-r)_0$ vs. M_r for galaxies in SCl A2142. Filled circles correspond to galaxies in rich groups, and empty circles show galaxies in poor groups (including single galaxies). The red circles correspond to the galaxies with old stellar populations ($D_n(4000) \geq 1.55$) and the blue circles to the galaxies having young stellar populations with $D_n(4000) < 1.55$. The green triangles show recently quenched galaxies with $D_n(4000) \leq 1.55$ and star formation rate $\log \text{SFR} < -0.5$. The red triangles indicate red, high SFR galaxies defined as $g-r \geq 0.7$, and $\log \text{SFR} \geq -0.5$. Orange stars represent AGNs. The dashed line shows the completeness limit $M_r = -19.6 + 5 \log_{10} h$.

infalling galaxies lie at large clustercentric distances and typically have velocity offsets around zero or with negative values (non-virialised region) with a small scatter (Dünner et al. 2007; Haines et al. 2015).

Galaxies with large clustercentric distances and positive velocity offsets may also be backsplash galaxies – galaxies which have passed cluster centre already at least once and now are orbiting at large clustercentric distances (Haines et al. 2015). For backsplash galaxies see also Bahé et al. (2013, and references therein).

The analysis of the PPS diagram has become an important tool to study galaxy populations in galaxy groups and clusters, to analyse dynamical properties of galaxies in clusters and outskirts and to compare galaxy populations in virialised and non-virialised regions of the clusters (Haines et al. 2015; Jaffé et al. 2015; Agulli et al. 2017; Paccagnella et al. 2017; Yoon et al. 2017; Rhee et al. 2017; Weinzirl et al. 2017).

We used projected phase space diagram for the main body of the A2142 supercluster to analyse the dynamical state of different galaxy groups in the supercluster, and their possible infall into the main cluster of the supercluster. We also used it to analyse the distribution of various galaxy populations in groups.

3.2. Substructure: normal mixture modelling

Multi-dimensional normal mixture modelling was used to search for substructure in galaxy groups. For this purpose we apply *mclust* package for classification and clustering (Fraley & Raftery 2006) from *R*, an open-source free statistical environment developed under the GNU GPL (Ihaka & Gentleman 1996, <http://www.r-project.org>). This package is based on the analysis of a finite mixture of distributions, in which each mixture component is taken to correspond to a different sub-group of the cluster. By default,

mclust analyses 14 different models with up to nine components. The best solution for components found by *mclust* is chosen using the Bayesian information criterion (BIC), the best solution has the highest value of BIC among all models and number of components considered by *mclust*. In *mclust* for every galaxy the probability to belong to any of the components is calculated, and the uncertainty of classification is defined as one minus the highest probability of a galaxy to belong to a component. Galaxies are assigned to components based on the highest probability calculated by *mclust*.

This analysis was applied only to groups that had more than 12 galaxies; for groups with a smaller number of galaxies the results of *mclust* are less reliable, as shown by Ribeiro et al. (2013). As an input for *mclust* we used the sky coordinates and velocity of the group member galaxies. The values of velocities were scaled to make them of the same order as the values of coordinates. In Einasto et al. (2012) and Einasto et al. (2018) this method was applied to analyse the substructure in galaxy groups and clusters. The same methodology was also used by Tempel et al. (2016a, 2017) to detect sub-components of friends-of-friends galaxy groups in order to refine group determination, and to find merging galaxy groups.

3.3. Magnitude gap between the brightest galaxies in groups

Magnitude gap between the brightest galaxies in groups is one indicator of the formation history of the groups and clusters, and their dynamical state (Kundert et al. 2017; Mulroy et al. 2017; Vitorelli et al. 2018, and references therein). Large magnitude gaps of the brightest galaxies in clusters suggests that such clusters may have formed earlier than groups and clusters with small magnitude gaps. They may also have different recent accretion history, groups or clusters with large magnitude gaps having larger time since the last major merger in them.

3.4. Orientations: group position angles, brightest galaxies, and supercluster axis

To determine the position angle of the supercluster axis and individual groups, we approximated their shape with the ellipse and found the position angle of its major axis. Details of this analysis were presented in Einasto et al. (2018). The position angle of the supercluster axis in Fig. 1 was determined by the distribution of rich galaxy groups in the supercluster (see also Einasto et al. 2018). The position angle of the supercluster axis is $63 \pm 1^\circ$, measured counterclockwise from west. Below we compare the orientation of the supercluster axis and galaxy groups, and check for the alignments between the brightest group galaxies, group and supercluster axes.

In the next two sections we analyse the galaxy content of galaxy groups in SCl A2142, and their location in the PPS diagram. The properties of individual groups are given in Appendix A.

4. Galaxy populations in groups

We analysed the full distributions of galaxy parameters in groups, and their median values. Our aim is to compare the galaxy content of groups in various locations in the supercluster, to see whether groups at different clustercentric radii in the supercluster main body and tail, and groups on the supercluster axis and off-axis groups have similar or different galaxy populations.

Table 2. Parameters of galaxies in groups.

(1)	(2)	(3)	(4)	(5)	(6)	(7)	(8)	(9)	(10)	(11)	(12)	(13)
No.	ID	$\log M^*$	F_h	$D_n(4000)$	$F_{1.55}$	$(g-r)_0$	F_{red}	SFR	F_p	t	F_{old}	$ \Delta M_{12} $
Main body		median		median		median		median		median		
1	10570	10.68	0.97	1.67	0.65	0.84 (0.85)	0.74 (0.74)	-0.44	0.48	3.0	0.52	0.04
2	3070	10.69	0.81	1.87	0.88	0.86	0.92	-1.29	0.87	8.3	0.77	1.24
3	4952	10.58	0.96	1.81	0.73	0.83 (0.83)	0.85 (0.82)	-0.98	0.59	4.4	0.59	0.33
4	32074	10.47	1.0	1.84	0.74	0.82	0.91	-1.20	0.73	5.5	0.73	0.17
5	35107	10.56	1.0	1.82	0.90	0.81	0.90	-1.15	0.90	4.5	0.90	0.18
6	14960	10.68	0.85	1.87	0.78	0.83 (0.84)	0.81 (0.83)	-1.21	0.70	5.0	0.63	0.58
7	17779	10.58	1.0	1.75	0.63	0.83	0.85	-1.04	0.60	4.6	0.63	0.0
8	6885	10.61	0.97	1.90	0.91	0.85	0.94	-1.35	0.93	8.4	0.81	0.39
9	21183	10.67	0.86	1.65	0.67	0.78	0.76	-0.72	0.62	3.8	0.57	0.04
Tail												
10	20324	10.44	0.73	1.85	0.82	0.84 (0.84)	0.91 (0.92)	-1.24	0.67	5.5	0.73	0.72
11	10818	10.72	0.93	1.89	0.79	0.86 (0.86)	0.86 (0.88)	-1.05	0.75	5.8	0.68	0.64
12	14283	10.52	0.89	1.80	0.68	0.83 (0.86)	0.85 (0.88)	-1.15	0.79	5.8	0.74	0.01
13	10224	10.82	0.95	1.90	0.81	0.84	0.90	-1.25	0.81	6.3	0.71	0.28
14	26895	10.63	0.83	1.76	0.82	0.82	0.92	-0.89	0.75	2.9	0.50	0.20
P(main)		10.59	0.85	1.68	0.60	0.80 (0.81)	0.72 (0.73)	-0.78	0.57	3.3	0.53	
P(tail)		10.54	0.84	1.67	0.55	0.80 (0.80)	0.69 (0.69)	-0.56	0.51	3.0	0.50	

Notes. Columns are as follows: (1): Order number of the group. P denotes galaxies in poor groups. Main mark galaxies in the main body of the supercluster up to clustercentric distances $11.5 h^{-1}$ Mpc, and tail - galaxies with clustercentric distances larger than $11.5 h^{-1}$ Mpc; (2): ID of the group; (3-12): Median values of galaxy parameters, and percentages of galaxies of high stellar mass, of old stellar populations according to the $D_n(4000)$ index, red galaxies, passive galaxies, and galaxies with old stellar ages in a group. Values in parenthesis show $(g-r)_0$ corresponding parameters calculated including colours of possible group members missing because of fibre collisions. (13) Magnitude gap between the two brightest galaxies in a group. For A2142 we give this for the BCG1 and BCG3 (Einasto et al. 2018).

We present median values of stellar masses ($\log M^*$), $D_n(4000)$ indexes, colours ($(g-r)_0$), SFRs (SFR), and stellar ages (t) of galaxies in rich groups in Table 2. Table 2 gives also the percentages of galaxies with old stellar populations according to the $D_n(4000)$ index, $F_{1.55}$, and stellar age, F_{old} , the percentage of red galaxies, F_{red} , passive galaxies, F_p , and the percentages of high stellar mass galaxies with stellar masses $\log M^* \geq 10.25$ (F_h , see Einasto et al. 2014, for the choice of this limit). For comparison we show parameters of galaxies in poor groups (denoted as P). For groups with galaxies missing due to the fibre collisions we give in Table 2 also the median value of colour index $(g-r)_0$ and percentages of red galaxies calculated including colours of possible group members. Table 2 shows that they only have minor effect. In Fig. 4 we show the sky distribution of galaxies from different populations. For each rich group we give the fraction of galaxies with old stellar populations according to the $D_n(4000)$ index, and the median stellar age (Table 2). Figure 4 gives a general picture of galaxy populations in groups in the supercluster.

Table 2 and Fig. 4 show that groups with the oldest stellar populations and lowest star formation rates reside in the cluster A2142 (Gr2), in Gr5 close to A2142, and in the group Gr8 on the supercluster axis at the edge of the main body of the supercluster where the supercluster tail begins. Approximately 90 % of galaxies in these groups have old stellar populations according to $D_n(4000)$ index. Also, according to the stellar age galaxies in A2142 cluster and Gr8 have median stellar populations older than 8 Gyr. Galaxy populations in the cluster A2142 and in its infalling subclusters were analysed in detail in Einasto et al. (2018). This analysis shows that galaxies with the oldest stellar populations and with the lowest star formation rates lie in the central, virialised region of A2142, and in one infalling subclus-

ter, called as M1 by Einasto et al. (2018). We compare M1 and Gr5 in Appendix A.

Groups on the supercluster axis have median ages of stellar populations approximately 4–7 Gyr, and the fraction of galaxies with old stellar populations 70–80 % (except Gr7 with 63% of old galaxies). In the supercluster main body groups with galaxies having the youngest stellar ages ($t < 4$ Gyr) and with the lowest percentages of galaxies with old stellar populations are Gr1 and Gr9 away from supercluster axis. The galaxy properties in these off-axis groups are more similar to those in poor groups which embed galaxies with younger stellar populations than rich groups in average. Groups with younger galaxy populations have also larger percentages of blue galaxies.

We used the Kolmogorov-Smirnov (KS) test to find the statistical significance of the differences in galaxy populations for galaxies in groups. We considered that the differences between distributions are highly significant if the p -value (the estimated probability of rejecting the hypothesis that distributions are statistically similar) is $p \leq 0.01$.

The statistical comparison of galaxy content of groups by individual groups is complicated due to small number of galaxies in groups with 12 or fewer member galaxies (four groups). In this case the results of the tests are not reliable, as shown, for example, in Ribeiro et al. (2013). Therefore, after initial comparison of galaxy content of groups we combined groups as follows. Groups 2, 5, and 8 can be taken together as the ones with the oldest stellar populations. The comparison of galaxy content of other groups shows that groups on the supercluster axis in the supercluster main body and in the tail do not have statistically significant differences between their galaxy populations, therefore groups 3, 4, 6, and 7 from the supercluster main body, together with groups 10–14 from the supercluster tail (notation Gr3-14

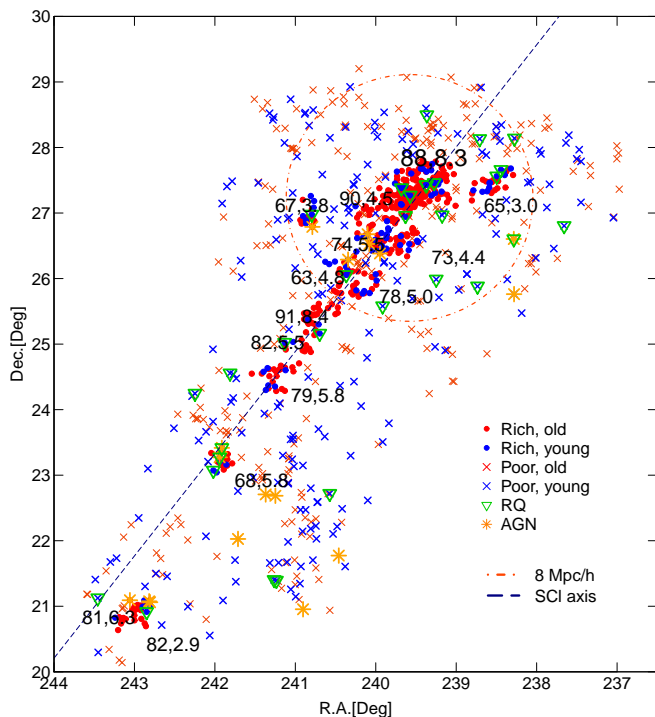


Fig. 4. Sky distribution of galaxies in SCI A2142. The red symbols show galaxies with old stellar populations ($D_n(4000) \geq 1.55$), and the blue symbols denote galaxies with young stellar populations ($D_n(4000) < 1.55$). The first number shows the percentage of galaxies with old stellar populations divided by $D_n(4000)$ index in rich groups. The second number shows the median age of galaxy populations in a group (in Gyr, Table 2). Galaxies in rich groups are denoted with filled circles. The crosses denote galaxies in poor groups with 2 – 9 galaxies, and single galaxies. The green triangles show recently quenched galaxies, and orange stars indicate the positions of AGNs. The orange circle has a radius of about $8 h^{-1}$ Mpc (in sky projection). The dashed line shows the supercluster axis.

from group ID-s, 3 - 14) form an on-axis group class. Off-axis groups Gr1 and Gr9 form a separate class (off-axis groups). Poor groups in the supercluster main body and tail have statistically similar galaxy populations and they can be taken together as one class of groups. In Fig. 5 we show the probability density distributions of $D_n(4000)$ index, $(g - r)_0$ colour index, and stellar masses $\log M^*$ for galaxies in groups from these divisions.

The KS test shows that the differences between $D_n(4000)$ indexes and colour indexes in the cluster A2142 and in Gr8 and Gr5 taken together, and in all other groups are significant at a very high level, with $p < 0.01$. Also, galaxy populations in groups on the supercluster axis and in off-axis groups are different at very high significance level, with $p < 0.01$.

Galaxies in the cluster A2142 and in Gr8 and Gr5 have higher stellar masses than galaxies in other groups (or in poor groups), with the KS test p -value $p \approx 0.01$. The stellar masses of galaxies in groups on the supercluster axis and in off-axis groups are statistically similar, with $p > 0.1$. This shows that galaxies with the same stellar mass in different groups have different star formation histories.

In Table 2 we also present the magnitude gaps of the brightest galaxies in SCI A2142 groups in r -band. The Table shows that the magnitude gap is larger than one magnitude in the cluster A2142 only. This suggests that the time since the last major merger in A2142 may be at least 4 Gyrs (Deason et al. 2013; Mulroy et al. 2017). The magnitude gaps between the brightest

galaxies in the cluster A2142 were analysed in more detail in Einasto et al. (2018). In other groups the magnitude gap is less than one magnitude, which indicates that groups are dynamically young.

5. Phase space diagram and clustercentric distances

Figure 6 presents the PPS diagram (velocity offset versus the projected clustercentric distance) for galaxies in different groups up to projected clustercentric distances $10.5 h^{-1}$ Mpc from the supercluster centre. Numbers show order numbers of groups from Table 1 where galaxies lie, and crosses indicate the positions of galaxies from poor groups or single galaxies. We also plot the location of recently quenched galaxies. Red star forming galaxies are mostly located in rich groups. We have not indicated them in Fig. 6 to avoid overcrowding figure. In the upper panel of Fig. 6 we show the probability density distributions of clustercentric distances of galaxies in rich and poor groups from various populations. The members of the cluster A2142 were not included in these calculations since their distribution was analysed in detail in Einasto et al. (2018). Distributions are normalised, so that each integrates to 1. We do not show error limits in the probability density distributions in upper panel of Fig. 6 since errors are sensitive to binning the data. We used full data (the integral distributions) to apply the Kolmogorov-Smirnov test for calculating the statistical significance of the differences between various distributions (see also comments on errors in Einasto et al. 2008).

Galaxies in Fig. 6 at projected clustercentric distances $D_c < 2 h^{-1}$ Mpc belong mostly to the cluster A2142, with virial radius of $0.9 h^{-1}$ Mpc and infall region of subclusters at radius of about $2 h^{-1}$ Mpc (Einasto et al. 2018). High peculiar velocities of galaxies indicate the Fingers-of-God effect. At higher clustercentric distances galaxies have mostly negative velocity offset in respect to the supercluster centre. They lie in the infall region of A2142 cluster. Thus all galaxies in the supercluster core may be falling into the main cluster. Of course, one must be cautious when interpreting observational data since we only have redshift information and sky coordinates of the galaxies. Also, as we show below, Gr8 is probably not falling into the main cluster.

Figure 6 reveals several interesting details about galaxies in the PPS diagram. Upper panel shows that the distributions of clustercentric distances of galaxies in rich groups have wide maxima at distances of about $2 - 4$ and $4 - 6 h^{-1}$ Mpc. Comparison with Fig. 1 shows that the maximum at $4 h^{-1}$ Mpc is formed by galaxies in groups Gr1 (1 in Table 1), Gr3, and Gr4. Together with A2142 they form the highest density core of the supercluster (Einasto et al. 2015). The maximum in clustercentric distance distribution at $5 - 6 h^{-1}$ Mpc is formed by groups Gr6, Gr7, and Gr9.

In Fig. 6 the distributions of clustercentric distances of galaxies in rich groups from old and young populations are shifted. In the distance interval up to $4 h^{-1}$ Mpc galaxies with old stellar populations lie closer to the main cluster than galaxies with young stellar populations. Galaxies with old stellar populations have a maximum in the clustercentric distance distribution at approximately $3 h^{-1}$ Mpc, while galaxies with young stellar populations have this maximum at $4 h^{-1}$ Mpc. The KS test shows that distance distributions of galaxies from different populations are statistically different with a high significance (p -values $p < 0.01$).

In poor groups the distribution of clustercentric distances of galaxies with young stellar populations has a maximum around

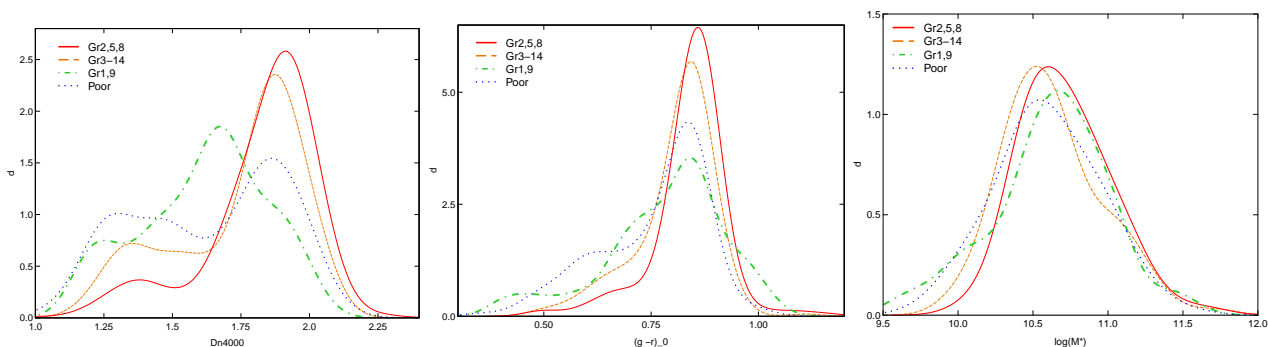


Fig. 5. Probability density distributions of $D_n(4000)$ index (left panel), $(g-r)_0$ colour index (middle panel), and stellar masses for galaxies (right panel) in groups 2, 5, and 8 (red solid line), groups 3, 4, 6, 7, and 10 - 14 (notation Gr3-14, orange dashed line), in groups 1 and 9 (green dot-dashed line), and in poor groups (blue dotted line). Group ID numbers are given in Table 1.

$6 h^{-1}$ Mpc. Figures 1 and 6 show that recently quenched galaxies mostly follow the distribution of galaxies in poor groups. Only 30% of these galaxies lie in rich groups. Of 13 recently quenched galaxies eight reside at clustercentric distances $5 - 7 h^{-1}$ Mpc. At this distance interval star-forming galaxies with young stellar populations and recently quenched galaxies are spread over the whole main body of the supercluster. They are neither preferentially located along the supercluster axis nor in filaments.

In the supercluster core up to clustercentric distances of $3 - 4 h^{-1}$ Mpc AGNs lie in a small region of the sky plane, in groups 3 and 4. Three of them are classified as AGNs in the SDSS database, and one is FR II radio galaxy. Other AGNs in the supercluster core lie at clustercentric distance interval $5 - 6 h^{-1}$ Mpc, in groups 7 and 9, and two of them are single galaxies. In the supercluster tail AGNs lie on groups 12, 13, and 14, and among poor groups in a lower density part of the tail. Their distribution follows the distribution of recently quenched galaxies.

Among red star-forming galaxies 60% lie in rich groups. We do not show them on the lower panel of Fig. 6, but present the distribution of their clustercentric distances in the upper panel of the figure. This distribution approximately follows that of galaxies in groups. The KS test shows that the distributions of clustercentric distances of red star forming galaxies, and galaxies in rich and poor groups are statistically similar, with p -value $p > 0.12$. This agrees with earlier findings that red star forming galaxies in superclusters can be found in groups of various richness, they may also be central galaxies of groups (Wolf et al. 2005; Einasto et al. 2008, 2014; Evans et al. 2018, and references therein).

6. Discussion

6.1. Collapse of the supercluster core

Einasto et al. (2015) and Gramann et al. (2015) applied the spherical collapse model to analyse the dynamical state of the main body of SCI 2142. The spherical collapse model describes the evolution of a spherically symmetric perturbation in an expanding universe. We summarise this model shortly in Appendix B. In this model the dynamics of a collapsing shell is determined by the mass in its interior. Einasto et al. (2015) and Gramann et al. (2015) defined a high-density core of the supercluster and its size using density contrasts in the luminosity-density field. They determined the dynamical mass embedded in regions with density above a certain threshold summing the dynamical masses of galaxy groups (Table 1 and Tempel et al.

2014b). For poor groups with $N_{\text{gal}} \leq 3$ they used the median values of masses of poor groups. Superclusters contain also intercluster gas which may form approximately 10% of their total mass (see e.g. Pompei et al. 2016). Total mass of the overdensity regions in the supercluster, M_{tot} , is obtained by adding this to the dynamical mass. This analysis showed that the high density core of SCI 2142 has already started to collapse.

For this study we calculated the mass - radius relation using different approach. The radial mass distribution is calculated using projected clustercentric radii. To determine the mass of the supercluster core at a given clustercentric radius we used group masses embedded into the core at this radius. For rich groups we use dynamical masses from Table 1. We find masses of poor groups using stellar mass-halo mass relation. According to this, the mass of the haloes can be calculated, employing the relation between the stellar mass M_* of the brightest galaxies in a group to halo mass M_{halo} from Moster et al. (2010),

$$\frac{M_*}{M_{\text{halo}}} = 2 \left(\frac{M_*}{M_{\text{halo}}} \right)_0 \left[\left(\frac{M_{\text{halo}}}{M_1} \right)^{-\beta} + \left(\frac{M_{\text{halo}}}{M_1} \right)^{\gamma} \right]^{-1}, \quad (3)$$

where $(M_*/M_{\text{halo}})_0 = 0.02817$ is the normalisation of the stellar to halo mass relation, the halo mass M_{halo} is the virial mass of haloes, $M_1 = 7.925 \times 10^{11} M_{\odot}$ is a characteristic mass, and $\beta = 1.068$ and $\gamma = 0.611$ are the slopes of the low- and high-mass ends of the relation, respectively. This method was used by Einasto et al. (2016) to find the mass of the Sloan Great Wall (SGW) superclusters, and by Lietzen et al. (2016) and Einasto et al. (2017) to estimate the mass of the BOSS Great Wall superclusters. The total mass was obtained summing the masses of groups and by adding 10% of the mass as the mass of gas in the supercluster.

We present the mass-radius relation for the main body of SCI 2142 in Fig. 7. Errors of the mass of a supercluster core at a given radius in Fig. 7 are calculated using group mass errors, which depend on the group richness (shaded regions in the figure). Einasto et al. (2016) estimate that, on average, supercluster mass errors due to group dynamical mass errors are of about 0.3 dex. For the core region of SCI A2142 such errors were probably overestimated. First, comparison of different mass estimates for the cluster A2142 showed that our mass estimate differs 4% only from those obtained in Munari et al. (2014) who compared several mass estimation methods. We used this as the error estimate of A2142 cluster mass. Comparison of dynamical mass estimates of groups with those obtained using stellar masses of groups brightest galaxies showed that in average, these estimates agree well although individual estimates

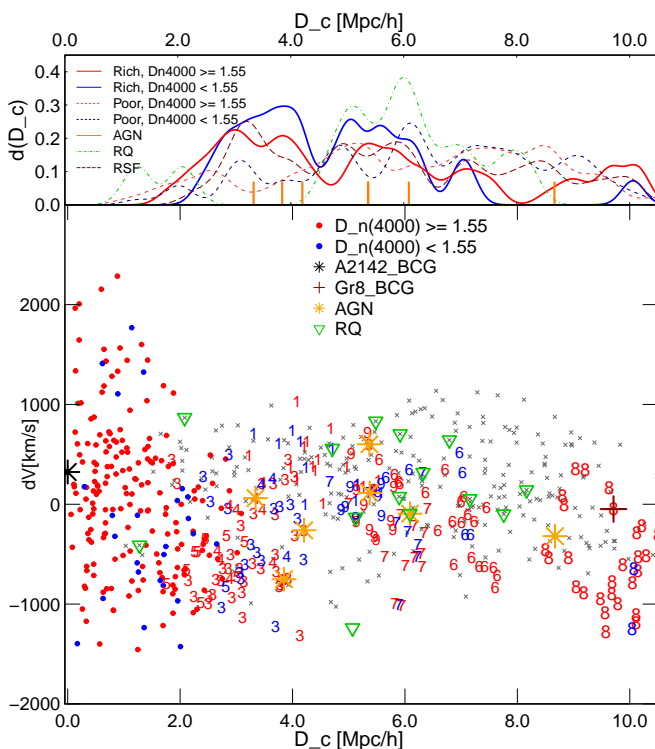


Fig. 6. Upper panel: Distribution of clustercentric distances for galaxies with young and old stellar populations in rich groups up to clustercentric distances $D_c \leq 10.5 h^{-1} \text{Mpc}$ (solid lines, $D_n(4000) \geq 1.55$), red line, and ($D_n(4000) < 1.55$), blue line), and in poor groups (dashed red and blue lines). Galaxies from the cluster A2142 are not included when calculating distributions. Green and dark red dashed lines show distribution of clustercentric distances of recently quenched and red star forming galaxies, respectively (see text for definition). Orange ticks show clustercentric distances of AGNs. Lower panel: Velocity of galaxies with respect to the cluster mean velocity vs. projected clustercentric distance for the supercluster A2142 main body up to clustercentric distances $D_c \leq 10.5 h^{-1} \text{Mpc}$ (PPS diagram). The red symbols show galaxies with old stellar populations ($D_n(4000) \geq 1.55$), and the blue symbols denote galaxies with young stellar populations ($D_n(4000) < 1.55$). Filled circles correspond to galaxies in the cluster A2142. Galaxies in other rich groups are plotted with the number which is the order number of a group in Table 1. Grey crosses indicate galaxies in poor groups with 2 – 9 galaxies, and single galaxies. Triangles show recently quenched galaxies, as in Fig. 1.

may differ up to 50% (Einasto et al. 2018). Therefore, for other rich groups with at least ten members galaxies we used 50% errors. For poor groups, for which we used the stellar masses of their brightest galaxies to calculate group masses, errors are of about 15%, obtained using errors of stellar mass estimates of galaxies (see Sect. 4.4 in Einasto et al. 2017, for details, dark shaded region in the figure). To compare different error estimates we show in Fig. 7 mass errors calculated using 50% errors for both rich and poor groups (except the cluster A2142) (light shaded region). Comparison of masses of SCI A2142 core regions obtained in this way (using both stellar masses and group dynamical masses) with masses calculated using group dynamical masses only shows that both estimates give very similar results (Einasto et al. 2015; Gramann et al. 2015). This suggests that we have no strong biases in the mass calculations. The same was concluded in Einasto et al. (2016) in which several mass estimates of the core regions of superclusters from the Sloan Great Wall were compared.

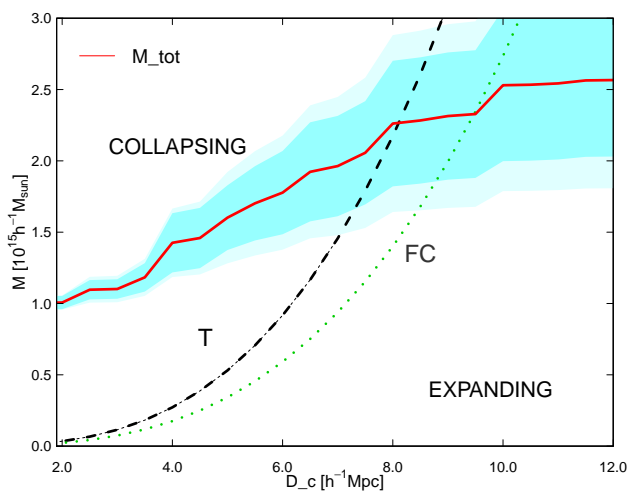


Fig. 7. Mass versus clustercentric distance for the main body of SCI 2142. Red solid line shows the total mass within a radius D_c , and shaded areas show error limits as explained in the text. Black and green dotted lines show turnaround (T) and future collapse (FC) mass ($M_T(R)$ and $M_{FC}(R)$) versus radius of a sphere R in a spherical collapse model (Appendix B).

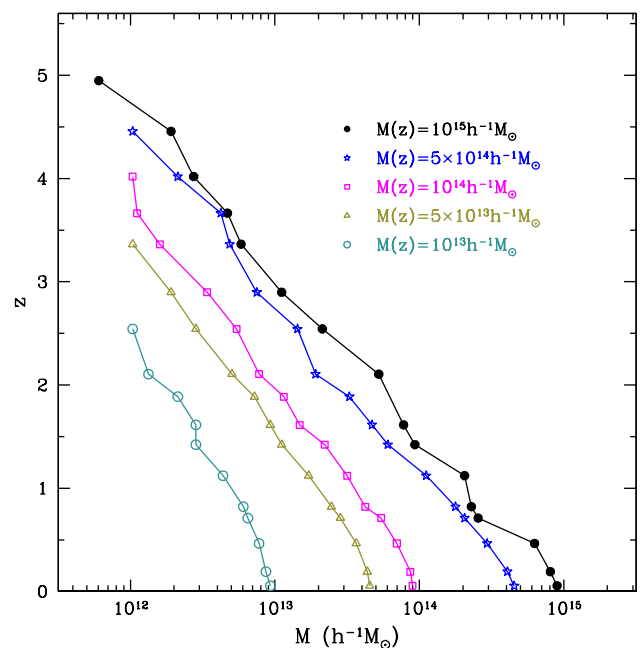


Fig. 8. Evolution of halo mass M with redshift z for five mass samples. Filled circles show the average evolutionary track of haloes with the current mass of $10^{15} h^{-1} M_\odot \pm 10\%$. Stars correspond to average mass $5 \times 10^{14} h^{-1} M_\odot$, open squares correspond to mass $10^{14} h^{-1} M_\odot$, open triangles to mass $5 \times 10^{13} h^{-1} M_\odot$, and open circles to mass $10^{13} h^{-1} M_\odot$.

At clustercentric distances up to approximately $3 h^{-1} \text{Mpc}$ the mass of the supercluster core is determined by the mass of the cluster A2142 and its infalling subclusters, including group Gr5 at clustercentric distance of $2.4 h^{-1} \text{Mpc}$. At clustercentric distances $3 - 4 h^{-1} \text{Mpc}$ the masses of groups Gr3 and Gr4 increase the mass of the supercluster core. According to Fig. 7, the radius of a region which has reached the turnaround and already started to collapse is of about $8 h^{-1} \text{Mpc}$. The total mass of the supercluster core within this clustercentric distance is $M_{\text{tot}} \approx 2.3 \times 10^{15} h^{-1} M_\odot$. The core of the supercluster with radius

of about $9 h^{-1}$ Mpc may collapse in the future. The total mass in the future collapse region is $M_{\text{tot}} \approx 2.4 \times 10^{15} h^{-1} M_{\odot}$.

Using simulations we are able to follow the evolution of dark matter haloes (Kim et al. 2015; Haines et al. 2018, and references therein). In Fig. 8 we present the mass evolution of simulated haloes found with FoF method in Horizon Run 4 simulations, as described in detail in Kim et al. (2015). The mass evolution of haloes with a given mass is plotted in Fig. 8 which shows the average evolutionary tracks of haloes with a given mass.

This figure shows that the increase of halo mass from high redshifts to the present depends on the halo mass. For example, the cluster-size haloes with current mass of $10^{15} h^{-1} M_{\odot}$ tend to have mass of about $10^{13} h^{-1} M_{\odot}$ at $z = 3$ on average. The half-mass period of cluster-size haloes with the present-day masses of about $M = 10^{15} h^{-1} M_{\odot}$ is at redshift $z = 0.5$. Approximately, we can use this relation to find how the mass of a collapsing core of the supercluster evolves with redshift. Using Appendix B and Eq. B.4 we find the radius of a collapsing core of the supercluster at this redshift. The overdensity of the turnaround at $z = 0.5$ is $\Delta\rho_T = 8.0$. Using this value, and the half of the mass of the core ($M = 1.15 \times 10^{15} h^{-1} M_{\odot}$), we obtain that the radius of the collapsing region at $z = 0.5$ was in comoving coordinates approximately $7.7 h^{-1}$ Mpc. At redshift $z = 1.0$ the masses of haloes had approximately five times lower values than their present-day masses. At this redshift the overdensity at the turnaround is $\Delta\rho_T = 6.6$ (Appendix B). We find that at redshift $z = 1.0$ the radius of a region which has reached turnaround and started to collapse was approximately $6 h^{-1}$ Mpc (in comoving coordinates). Its mass was $M \approx 5 \times 10^{14} h^{-1} M_{\odot}$.

The mass and radius of the collapsing core of SCI 2142 are larger than those in the collapsing cores in the SGW superclusters. In the SGW superclusters the mass of the most massive core which has reached turnaround is $M \approx 1.8 \times 10^{15} h^{-1} M_{\odot}$ (Einasto et al. 2016). The radii of collapsing cores in other superclusters do not exceed $10 h^{-1}$ Mpc (Reisenegger et al. 2000; Pearson et al. 2014; O’Mill et al. 2015; Chon et al. 2015). Reisenegger et al. (2000) and Pearson et al. (2014) showed that only very massive collapsing supercluster cores with a number of rich galaxy clusters as in the Shapley supercluster and in the Corona Borealis supercluster, and perhaps in the rich protosupercluster at redshift $z = 2.45$ (Cucciati et al. 2018) may be larger and more massive.

6.2. SCI A2142 and the evolution of clusters and superclusters

In this study we find that the main cluster of SCI 2142, A2142, and the group Gr8 at the edge of the supercluster main body are populated by the oldest galaxies among groups in the supercluster. The median age of galaxies in them is higher than 8 Gyr. We may suppose that these systems and their galaxies had already started to form in a very early universe together with first galaxies observed at high redshifts (Chiang et al. 2017; Muldrew et al. 2018; Marrone et al. 2018; Pavese et al. 2018).

The radius of a collapsing region around Gr8 with mass of about $M = 1.6 \times 10^{14} h^{-1} M_{\odot}$ is $R_T \approx 3.3 h^{-1}$ Mpc. The radius of the collapsing core of A2142 is $R_T \approx 8 h^{-1}$ Mpc. As the mass of the cluster A2142 is much higher than that of Gr8, it is in a much deeper potential well and during the evolution, much more galaxies from a larger volume fall into A2142 than into Gr8 making it richer than Gr8. Simulations show that present-day clusters with mass of about $M \approx 10^{15} h^{-1} M_{\odot}$ as the cluster A2142 and $M \approx 10^{14} h^{-1} M_{\odot}$ as the group Gr8 had comoving effective radii at redshift $z = 0.5$ approximately 4 and $1.5 h^{-1}$ Mpc, and approx-

imately 10 and $5 h^{-1}$ Mpc at redshift $z = 1$ (Chiang et al. 2013). At higher redshifts galaxies may fall into forming clusters even from larger volumes (Muldrew et al. 2018).

The collapsing core in the supercluster, infalling subclusters and groups around the cluster A2142, and possible group merging, found in this study and in Einasto et al. (2018) show that the evolution of the supercluster and its members continues. Multi-wavelength studies of the cluster A2142 have revealed substructure in the cluster, and infalling galaxies and groups which affect the galaxy properties in the cluster (Markevitch et al. 2000; Eckert et al. 2014, 2017; Venturi et al. 2017; Einasto et al. 2018; Liu et al. 2018). It is possible that during the future evolution all groups in the core of SCI A2142 join the main cluster, as predicted by simulations about the future evolution of superclusters (Araya-Melo et al. 2009). At present, we evidence one epoch in this evolution.

Galaxy groups in lower density regions have higher fraction of star-forming galaxies than galaxies in superclusters (Lietzen et al. 2012; Einasto et al. 2014). Therefore we could expect that the percentage of star-forming galaxies increases with distance from the supercluster centre along the supercluster axis. We did not find statistically significant differences between groups in the supercluster core and in the tail. However, the galaxy content of other groups in SCI 2142 depends on the location of groups with respect to the supercluster axis. Groups on the supercluster axis hosts galaxies that have older galaxy populations than groups which lie away from the supercluster axis, having median ages of about 4 – 6 Gyr and less than 4 Gyr, correspondingly. The supercluster axis present a preferred direction for the group and galaxy infall into the main cluster (Einasto et al. 2018). This may affect galaxy content of groups and cause also an alignment signal for some infalling groups. In the core of SCI A2142 the most elongated group, Gr4, and its brightest galaxy are aligned along the supercluster axis. Recent discussion and references about the galaxy and cluster alignments in the cosmic web can be found in Einasto et al. (2018), and in Ganeshiah Veena et al. (2018).

Bianconi et al. (2018) analysed the galaxy content of groups infalling into massive clusters at redshifts $0.15 < z < 0.3$. Their study showed that the star formation quenching is effective in groups before infalling to clusters. Our study tells us that the star formation history in galaxies also depends on the location of galaxies and groups in the cosmic web. Detailed dynamical study with precise peculiar velocity and mass estimates are needed to understand the details of the evolution of clusters and superclusters, and their dynamics.

6.3. Star-forming and recently quenched galaxies and AGNs

Star-forming galaxies in groups of SCI A2142 are located approximately at the virial radii of groups, or near the edge of groups. In merging groups these galaxies lie in the zone where galaxies from merging groups overlap in the PPS diagram (see below, and also in Appendix A). Up to clustercentric distances $4 h^{-1}$ Mpc the distribution of clustercentric distances of star-forming galaxies in rich groups is peaked at higher distances than that of galaxies with old stellar populations. We find the enhanced fraction of star forming and recently quenched galaxies at clustercentric distances of about $6 - 8 h^{-1}$ Mpc, especially in poor groups. This is the borderline of the turnaround region of the supercluster core. In addition, several AGN host galaxies are recently quenched, or they lie close to recently quenched galaxies.

In the cold dark matter hierarchical structure formation models, galaxy clusters grow by accreting matter (galaxies, groups, and gas) from their surroundings. Simulations predict the existence of large-scale accretion shocks between the virial and turnaround radii of clusters of galaxies (Molnar et al. 2009; Kocsis et al. 2005). The densest and hottest shocks occur at the intersections of filaments around the locations of clusters of galaxies (Loeb & Waxman 2000). Ebeling et al. (2014) found that gas-rich galaxies possibly shocked by infalling into the cluster or by the passage of a shock wave can exhibit high star-formation rates. Using Fermi-LAT and ROSAT data, signatures of virial rings around Coma cluster and the cumulative γ -ray emission from accretion shocks of stacked 112 rich clusters were recently detected (Keshet 2017; Reiss & Keshet 2018).

Keshet et al. (2018) showed a presence of a γ -ray excess due to the virial shock near the virial radius of the cluster A2142. Einasto et al. (2018) found that star-forming and recently quenched galaxies in this cluster are located at the infall region of subclusters, approximately at the same radius as detected by Keshet et al. (2018) as the radius of a virial shock. Einasto et al. (2018) concluded that mergers and infall of subclusters affect the properties of galaxies and lead to rapid changes in galaxy properties. As shown by Keshet et al. (2018), this is accompanied by a virial ring at high energies.

Several AGNs lie at the clustercentric distances of about $4 h^{-1}$ Mpc. Among them there is one FR II galaxy. At these distances we did not find any recently quenched galaxy. Stroe et al. (2015) and Sobral et al. (2015) found that shock waves in merging clusters can trigger the star formation and AGN activity in galaxies for a short time, of order of 100 Myr. Bird et al. (2008) showed that average FR II lifetime in groups is even shorter, $15(\pm 5) \times 10^6$ years. The absence of recently quenched galaxies at $D_c \approx 4 h^{-1}$ Mpc may be due to the short timescale at which shock waves trigger the star formation in galaxies (Stroe et al. 2015; Sobral et al. 2015). Radio lobes of the FR II galaxy in Gr3 are aligned along the supercluster axis (see Fig. A.1 in Capetti et al. 2017). However, this may be a coincidence. To understand this, studies of the co-evolution of the structures of different scales from active nuclei in galaxies to groups and superclusters of galaxies are needed.

The distributions of clustercentric distances of galaxies with old and young populations in groups are shifted, galaxies with old stellar populations lie at lower clustercentric distances than galaxies with young stellar populations. This may be an indication that stellar populations in galaxies closer to the main cluster were quenched earlier than those in galaxies farther away.

In groups Gr8, Gr12, and Gr13 (Figs. A.3 - A.5) star-forming galaxies and AGNs are located approximately at the virial radius of a group, near the edge of a group, or they lie in the zone where galaxies from possibly merging groups overlap. Einasto et al. (2018) found that in the cluster A2142 star-forming galaxies lie in the infall zone of subclusters. This has also been found in other studies. For example, Deshev et al. (2017) have detected a high percentage of star-forming galaxies in the cluster A520 in infalling groups at high clustercentric distances. Braglia et al. (2009) and Mahajan et al. (2012) showed that in dynamically unrelaxed clusters the average star formation history of cluster member galaxies depends both on clustercentric distance of galaxies, and on cluster substructure. Baxter et al. (2017) found that colours of galaxies from the SDSS change at the halo boundaries. This may be evidence of merger-induced star formation in galaxies. Aragon-Calvo et al. (2016) associate the changes in star formation properties of galaxies with cosmic web detachment as galaxies fall into clusters.

Possible merger-induced star formation in galaxies along filaments between clusters have been reported by Johnston-Hollitt et al. (2008) who found an excess of blue star-forming galaxies in the filament which connects clusters in the core region of the Horologium-Reticulum supercluster. An excess of star-forming galaxies have also been found in filaments surrounding other galaxy clusters (Porter & Raychaudhury 2007; Braglia et al. 2007; Porter et al. 2008; Fadda et al. 2008; Edwards et al. 2010).

We find an excess of star-forming galaxies, recently quenched galaxies, and AGNs at clustercentric distances of about $6 h^{-1}$ Mpc. This is more clearly seen in the distribution of galaxies from poor groups. At this distance star-forming and recently quenched galaxies are spread over the whole main body of the supercluster. They are not located preferentially along the supercluster axis or in filaments in the supercluster main body. We could expect that star-forming galaxies lie in the outer parts of the supercluster main body, so that the fraction of star-forming galaxies increases with clustercentric distance. The increase of the fraction of star-forming galaxies around clusters have been found in several other studies (Bahé et al. 2013; Haines et al. 2015). Opposite to this, in outskirts of SCI A2142 main body the fraction of star-forming galaxies decreases. The origin of the excess at $D_c \approx 6 h^{-1}$ Mpc is not yet clear.

7. Summary

We analysed the structure, dynamical state, and galaxy content of the supercluster SCI 2142. Our main results are as follows.

- 1) The total mass of the collapsing core of the supercluster is $M_{\text{tot}} \approx 2.3 \times 10^{15} h^{-1} M_{\odot}$, and its radius is approximately $8 h^{-1}$ Mpc. Groups in the supercluster core up to clustercentric distances of about $8 h^{-1}$ Mpc are infalling into the main cluster.
- 2) Stellar populations in galaxies in groups on the supercluster axis are older than in off-axis groups, with median stellar ages of 4 – 6 (on-axis groups) and < 4 Gyr (off-axis groups). Populations in poor groups have median ages of order of 3 Gyr. Stellar populations are the oldest (with median stellar age $t > 8$ Gyr) in galaxies in the central cluster, A2142, and group Gr8 at the clustercentric distance of about $10 h^{-1}$ Mpc.
- 3) Group Gr5 with its small clustercentric distance and galaxy populations similar to populations in the cluster A2142 and its infalling subcluster may be a part of a small filament infalling into the cluster A2142.
- 4) The small magnitude gap between the brightest galaxies in groups, substructure, infall, and merging of groups suggest that galaxy groups in SCI A2142 are dynamically young.
- 5) There is an excess of star-forming and recently quenched galaxies and AGNs in poor groups at the clustercentric distances $D_c \approx 6 h^{-1}$ Mpc.

The progenitors of the cluster A2142 might be similar to rare, very rich protoclusters which are now observed at high redshifts. The cluster is embedded in a supercluster with unusual morphology among superclusters, having almost spherical, collapsing main body and straight tail (Einasto et al. 2015). The collapsing core of the supercluster, dynamically young galaxy groups in it, infall of galaxies and groups, and their possible merging which affect galaxy properties, as found in this and earlier studies (see references in Sect. 6.2), show how the whole supercluster is evolving. To check whether the abundance and evolution of very rich clusters and superclusters is compatible with the current cosmological model we need to analyse halo properties in

very large-volume simulation like the Horizon Run 4 simulations (Kim et al. 2015). It is necessary to analyse a large sample of galaxy superclusters and galaxies and groups in them to better understand the coevolution of different structures in the cosmic web.

Acknowledgements. We thank the referee for suggestions and comments that helped to improve the paper. We are pleased to thank the SDSS Team for the publicly available data releases. Funding for the Sloan Digital Sky Survey (SDSS) and SDSS-II has been provided by the Alfred P. Sloan Foundation, the Participating Institutions, the National Science Foundation, the U.S. Department of Energy, the National Aeronautics and Space Administration, the Japanese Monbukagakusho, and the Max Planck Society, and the Higher Education Funding Council for England. The SDSS website is <http://www.sdss.org/>. The SDSS is managed by the Astrophysical Research Consortium (ARC) for the Participating Institutions. The Participating Institutions are the American Museum of Natural History, Astrophysical Institute Potsdam, University of Basel, University of Cambridge, Case Western Reserve University, The University of Chicago, Drexel University, Fermilab, the Institute for Advanced Study, the Japan Participation Group, The Johns Hopkins University, the Joint Institute for Nuclear Astrophysics, the Kavli Institute for Particle Astrophysics and Cosmology, the Korean Scientist Group, the Chinese Academy of Sciences (LAMOST), Los Alamos National Laboratory, the Max-Planck-Institute for Astronomy (MPIA), the Max-Planck-Institute for Astrophysics (MPA), New Mexico State University, Ohio State University, University of Pittsburgh, University of Portsmouth, Princeton University, the United States Naval Observatory, and the University of Washington. The present study was supported by the ETAG projects IUT26-2 and IUT40-2, by the European Structural Funds grant for the Centre of Excellence "Dark Matter in (Astro)particle Physics and Cosmology" TK133, and by grant MOBTP86. HL is funded by PUT1627 grant from Estonian Research Council. This work was partially supported by the Supercomputing Center/Korea Institute of Science and Technology Information with supercomputing resources including technical support (KSC-2013-G2-003). JK and CP thank Korea Institute for Advanced Study for providing computing resources (KIAS Center for Advanced Computation) for the analysis of the HR4 data. This work has also been supported by ICRANet through a professorship for Jaan Einasto.

References

- Agulli, I., Aguerri, J. A. L., Diaferio, A., Dominguez Palmero, L., & Sánchez-Janssen, R. 2017, *MNRAS*, 467, 4410
- Ahn, C. P., Alexandroff, R., Allende Prieto, C., et al. 2014, *ApJS*, 211, 17
- Aihara, H., Allende Prieto, C., An, D., et al. 2011, *ApJS*, 193, 29
- Aragon-Calvo, M. A., Neyrinck, M. C., & Silk, J. 2016, *ArXiv e-prints* [arXiv:1607.07881]
- Araya-Melo, P. A., Reisenegger, A., Meza, A., et al. 2009, *MNRAS*, 399, 97
- Bahé, Y. M., McCarthy, I. G., Balogh, M. L., & Font, A. S. 2013, *MNRAS*, 430, 3017
- Balogh, M. L., Morris, S. L., Yee, H. K. C., Carlberg, R. G., & Ellingson, E. 1999, *ApJ*, 527, 54
- Baxter, E., Chang, C., Jain, B., et al. 2017, *ApJ*, 841, 18
- Bianconi, M., Smith, G. P., Haines, C. P., et al. 2018, *MNRAS*, 473, L79
- Bird, J., Martini, P., & Kaiser, C. 2008, *ApJ*, 676, 147
- Blanton, M. R., Hogg, D. W., Bahcall, N. A., et al. 2003, *ApJ*, 592, 819
- Blanton, M. R. & Roweis, S. 2007, *AJ*, 133, 734
- Bond, J. R., Kofman, L., & Pogosyan, D. 1996, *Nature*, 380, 603
- Braglia, F., Pierini, D., & Böhringer, H. 2007, *A&A*, 470, 425
- Braglia, F. G., Pierini, D., Biviano, A., & Böhringer, H. 2009, *A&A*, 500, 947
- Brinchmann, J., Charlot, S., White, S. D. M., et al. 2004, *MNRAS*, 351, 1151
- Bruzual, G. & Charlot, S. 2003, *MNRAS*, 344, 1000
- Capetti, A., Massaro, F., & Baldi, R. D. 2017, *A&A*, 601, A81
- Cautun, M., van de Weygaert, R., Jones, B. J. T., & Frenk, C. S. 2014, *MNRAS*, 441, 2923
- Chiang, Y.-K., Overzier, R., & Gebhardt, K. 2013, *ApJ*, 779, 127
- Chiang, Y.-K., Overzier, R. A., Gebhardt, K., & Henriques, B. 2017, *ApJL*, 844, L23
- Chiueh, T. & He, X.-G. 2002, *Phys. Rev. D*, 65, 123518
- Chon, G., Böhringer, H., & Zaroubi, S. 2015, *A&A*, 575, L14
- Cucciati, O., Lemaux, B. C., Zamorani, G., et al. 2018, *ArXiv e-prints* [arXiv:1806.06073]
- Deason, A. J., Conroy, C., Wetzel, A. R., & Tinker, J. L. 2013, *ApJ*, 777, 154
- Deshev, B., Finoguenov, A., Verdugo, M., et al. 2017, *A&A*, 607, A131
- Duarte, M. & Mamon, G. A. 2015, *MNRAS*, 453, 3848
- Dünner, R., Araya, P. A., Meza, A., & Reisenegger, A. 2006, *MNRAS*, 366, 803
- Dünner, R., Reisenegger, A., Meza, A., Araya, P. A., & Quintana, H. 2007, *MNRAS*, 376, 1577
- Ebeling, H., Stephenson, L. N., & Edge, A. C. 2014, *ApJL*, 781, L40
- Eckert, D., Gaspari, M., Owers, M. S., et al. 2017, *A&A*, 605, A25
- Eckert, D., Molendi, S., Owers, M., et al. 2014, *A&A*, 570, A119
- Edwards, L. O. V., Fadda, D., Frayer, D. T., Lima Neto, G. B., & Durret, F. 2010, *AJ*, 140, 1891
- Einasto, M., Deshev, B., Lietzen, H., et al. 2018, *A&A*, 610, A82
- Einasto, M., Gramann, M., Saar, E., et al. 2015, *A&A*, 580, A69
- Einasto, M., Lietzen, H., Gramann, M., et al. 2017, *A&A*, 603, A5
- Einasto, M., Lietzen, H., Gramann, M., et al. 2016, *A&A*, 595, A70
- Einasto, M., Lietzen, H., Tempel, E., et al. 2014, *A&A*, 562, A87
- Einasto, M., Saar, E., Martínez, V. J., et al. 2008, *ApJ*, 685, 83
- Einasto, M., Vennik, J., Nurmi, P., et al. 2012, *A&A*, 540, A123
- Evans, F. A., Parker, L. C., & Roberts, I. D. 2018, *MNRAS*, 476, 5284
- Fadda, D., Biviano, A., Marleau, F. R., Storrie-Lombardi, L. J., & Durret, F. 2008, *ApJL*, 672, L9
- Fräley, C. & Raftery, A. E. 2006, Technical Report, Dep. of Statistics, University of Washington, 504, 1
- Ganeshaiha Veena, P., Cautun, M., van de Weygaert, R., et al. 2018, *MNRAS*, 481, 414
- Gramann, M., Einasto, M., Heinämäki, P., et al. 2015, *A&A*, 581, A135
- Haines, C. P., Finoguenov, A., Smith, G. P., et al. 2018, *MNRAS*, 477, 4931
- Haines, C. P., Iovino, A., Krywult, J., et al. 2017, *A&A*, 605, A4
- Haines, C. P., Pereira, M. J., Smith, G. P., et al. 2015, *ApJ*, 806, 101
- Huchra, J. P. & Geller, M. J. 1982, *ApJ*, 257, 423
- Ihaka, R. & Gentleman, R. 1996, *Journal of Computational and Graphical Statistics*, 5, 299
- Jöeveer, M. & Einasto, J. 1978, in *IAU Symposium, Vol. 79, Large Scale Structures in the Universe*, ed. M. S. Longair & J. Einasto, 241–250
- Jöeveer, M., Einasto, J., & Tago, E. 1978, *MNRAS*, 185, 357
- Jaffé, Y. L., Smith, R., Candlish, G. N., et al. 2015, *MNRAS*, 448, 1715
- Johnston-Hollitt, M., Sato, M., Gill, J. A., Fleenor, M. C., & Brick, A.-M. 2008, *MNRAS*, 390, 289
- Kauffmann, G., Heckman, T. M., White, S. D. M., et al. 2003a, *MNRAS*, 341, 33
- Kauffmann, G., Heckman, T. M., White, S. D. M., et al. 2003b, *MNRAS*, 341, 54
- Keshet, U. 2017, in *Proceedings of the 7th International Fermi Symposium, held 15-20 October 2017, in Garmisch-Partenkirchen, Germany (IFS2017)*. Online at https://pos.sissa.it/cgi-bin/reader/conf.cgi?confid=312, id.151, 151
- Keshet, U., Reiss, I., & Hurier, G. 2018, *ArXiv e-prints* [arXiv:1801.01494]
- Kim, J., Park, C., L'Huillier, B., & Hong, S. E. 2015, *Journal of Korean Astronomical Society*, 48, 213
- Kocsis, B., Haiman, Z., & Frei, Z. 2005, *ApJ*, 623, 632
- Kofman, L. A. & Shandarin, S. F. 1988, *Nature*, 334, 129
- Komatsu, E., Smith, K. M., Dunkley, J., et al. 2011, *ApJS*, 192, 18
- Kravtsov, A. V. & Borgani, S. 2012, *ARA&A*, 50, 353
- Kundert, A., D'Onghia, E., & Aguerri, J. A. L. 2017, *ApJ*, 845, 45
- Lahav, O., Lilje, P. B., Primack, J. R., & Rees, M. J. 1991, *MNRAS*, 251, 128
- Lietzen, H., Tempel, E., Heinämäki, P., et al. 2012, *A&A*, 545, A104
- Lietzen, H., Tempel, E., Liivamägi, L. J., et al. 2016, *A&A*, 588, L4
- Liivamägi, L. J., Tempel, E., & Saar, E. 2012, *A&A*, 539, A80
- Liu, A., Yu, H., Diaferio, A., et al. 2018, *ApJ*, 863, 102
- Loeb, A. & Waxman, E. 2000, *Nature*, 405, 156
- Lovell, C. C., Thomas, P. A., & Wilkins, S. M. 2018, *MNRAS*, 474, 4612
- Mahajan, S., Raychaudhury, S., & Pimblett, K. A. 2012, *MNRAS*, 427, 1252
- Maraston, C., Strömbäck, G., Thomas, D., Wake, D. A., & Nichol, R. C. 2009, *MNRAS*, 394, L107
- Markevitch, M., Ponman, T. J., Nulsen, P. E. J., et al. 2000, *ApJ*, 541, 542
- Marrone, D. P., Spilker, J. S., Hayward, C. C., et al. 2018, *Nature*, 553, 51
- Martínez, V. J. & Saar, E. 2002, *Statistics of the Galaxy Distribution* (Chapman & Hall/CRC, Boca Raton)
- Molnar, S. M., Hearn, N., Haiman, Z., et al. 2009, *ApJ*, 696, 1640
- Moster, B. P., Somerville, R. S., Maudsells, C., et al. 2010, *ApJ*, 710, 903
- Muldrew, S. I., Hatch, N. A., & Cooke, E. A. 2018, *MNRAS*, 473, 2335
- Mulroy, S. L., McGee, S. L., Gillman, S., et al. 2017, *MNRAS*, 472, 3246
- Munari, E., Biviano, A., & Mamon, G. A. 2014, *A&A*, 566, A68
- Muzzin, A., van der Burg, R. F. J., McGee, S. L., et al. 2014, *ApJ*, 796, 65
- Old, L., Skibba, R. A., Pearce, F. R., et al. 2014, *MNRAS*, 441, 1513
- Old, L., Wojtak, R., Mamon, G. A., et al. 2015, *MNRAS*, 449, 1897
- Old, L., Wojtak, R., Pearce, F. R., et al. 2018, *MNRAS*, 475, 853
- Oman, K. A., Hudson, M. J., & Behroozi, P. S. 2013, *MNRAS*, 431, 2307
- O'Mill, A. L., Proust, D., Capelato, H. V., et al. 2015, *MNRAS*, 453, 868
- Overzier, R. A. 2016, *A&A Rev.*, 24, 14
- Owers, M. S., Nulsen, P. E. J., & Couch, W. J. 2011, *ApJ*, 741, 122
- Paccagnella, A., Vulcani, B., Poggianti, B. M., et al. 2017, *ApJ*, 838, 148
- Pavesi, R., Riechers, D. A., Sharon, C. E., et al. 2018, *ApJ*, 861, 43
- Pearson, D. W., Batista, M., & Batuski, D. J. 2014, *MNRAS*, 441, 1601
- Peebles, P. J. E. 1980, *The large-scale structure of the universe* (Princeton University Press)

- Peebles, P. J. E. 1984, *ApJ*, 284, 439
- Pompei, E., Adami, C., Eckert, D., et al. 2016, *A&A*, 592, A6
- Porter, S. C. & Raychaudhury, S. 2007, *MNRAS*, 375, 1409
- Porter, S. C., Raychaudhury, S., Pimblett, K. A., & Drinkwater, M. J. 2008, *MNRAS*, 388, 1152
- Proust, D., Quintana, H., Carrasco, E. R., et al. 2006, *A&A*, 447, 133
- Reisenegger, A., Quintana, H., Carrasco, E. R., & Maze, J. 2000, *AJ*, 120, 523
- Reiss, I. & Keshet, U. 2018, *J. Cosmology Astropart. Phys.*, 10, 010
- Rhee, J., Smith, R., Choi, H., et al. 2017, *ApJ*, 843, 128
- Ribeiro, A. L. B., de Carvalho, R. R., Trevisan, M., et al. 2013, *MNRAS*, 434, 784
- Salim, S., Rich, R. M., Charlot, S., et al. 2007, *ApJS*, 173, 267
- Small, T. A., Ma, C.-P., Sargent, W. L. W., & Hamilton, D. 1998, *ApJ*, 492, 45
- Sobral, D., Stroe, A., Dawson, W. A., et al. 2015, *MNRAS*, 450, 630
- Stroe, A., Sobral, D., Dawson, W., et al. 2015, *MNRAS*, 450, 646
- Suhhonenko, I., Einasto, J., Liivamägi, L. J., et al. 2011, *A&A*, 531, A149
- Tempel, E., Einasto, J., Einasto, M., Saar, E., & Tago, E. 2009, *A&A*, 495, 37
- Tempel, E., Kipper, R., Tamm, A., et al. 2016a, *A&A*, 588, A14
- Tempel, E., Stoica, R. S., Kipper, R., & Saar, E. 2016b, *Astronomy and Computing*, 16, 17
- Tempel, E., Stoica, R. S., Martínez, V. J., et al. 2014a, *MNRAS*, 438, 3465
- Tempel, E., Tago, E., & Liivamägi, L. J. 2012, *A&A*, 540, A106
- Tempel, E., Tamm, A., Gramann, M., et al. 2014b, *A&A*, 566, A1
- Tempel, E., Tuvikene, T., Kipper, R., & Libeskind, N. I. 2017, *A&A*, 602, A100
- Toshikawa, J., Kashikawa, N., Overzier, R., et al. 2016, *ApJ*, 826, 114
- Tremonti, C. A., Heckman, T. M., Kauffmann, G., et al. 2004, *ApJ*, 613, 898
- van de Weygaert, R. & Schaap, W. 2009, in *Lecture Notes in Physics*, Berlin Springer Verlag, Vol. 665, *Data Analysis in Cosmology*, ed. V. J. Martínez, E. Saar, E. Martínez-González, & M.-J. Pons-Bordería, 291–413
- Venturi, T., Rossetti, M., Brunetti, G., et al. 2017, *A&A*, 603, A125
- Vitorelli, A. Z., Cypriano, E. S., Makler, M., et al. 2018, *MNRAS*, 474, 866
- Weinzirl, T., Aragón-Salamanca, A., Gray, M. E., et al. 2017, *MNRAS*, 471, 182
- Wojtak, R., Old, L., Mamon, G. A., et al. 2018, *MNRAS*, 481, 324
- Wolf, C., Gray, M. E., & Meisenheimer, K. 2005, *A&A*, 443, 435
- Wu, H.-Y., Hahn, O., Wechsler, R. H., Mao, Y.-Y., & Behroozi, P. S. 2013, *ApJ*, 763, 70
- Yoon, H., Chung, A., Smith, R., & Jaffé, Y. L. 2017, *ApJ*, 838, 81
- Zeldovich, I. B., Einasto, J., & Shandarin, S. F. 1982, *Nature*, 300, 407

Appendix A: Individual galaxy groups

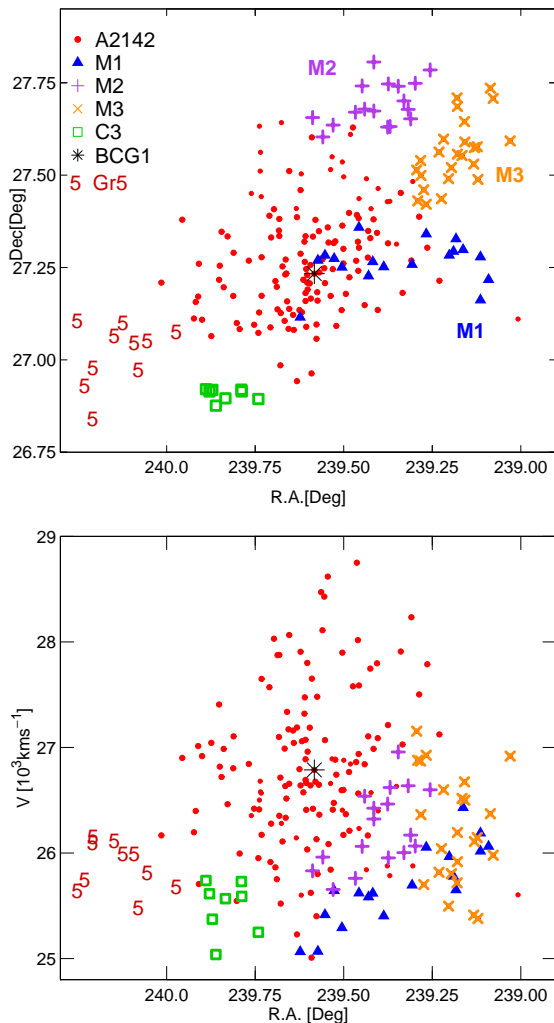


Fig. A.1. Distribution of galaxies in three components of the cluster A2142 and in the group Gr5 in the sky plane (upper panel) and in the R.A. - velocity plane (lower panel). Red symbols correspond to the galaxies in the main component of A2142, C1. Blue, violet, and orange symbols show galaxies from infalling subclusters M1, M2, and M3 (see text), and green symbols denote the location of galaxies from the third component, C3. Black star indicates the location of the brightest cluster galaxy (BCG1).

Below we describe the properties of individual groups with at least ten member galaxies, their substructure, dynamical state, orientation, the location of star forming galaxies and AGNs in a group, and possible group merging. For each group we present an analysis relevant to this particular group. For example, we search for possible substructure in groups with more than 12 galaxies only, for groups with smaller number of galaxies the results of *mclust* are less reliable, as shown by Ribeiro et al. (2013). If we identify AGNs in a group we note their location, but AGNs have not been found in every group. For two groups we present the PPS diagrams with galaxies from neighbouring poor groups and discuss the possibility that groups may be merging.

Group Gr5, a small group of ten galaxies, is the closest group to the main cluster of the supercluster, A2142. Einasto et al. (2018) found that the cluster A2142 has three infalling subclusters, named M1, M2, and M3, and a poor infalling group called as C3. Subclusters M1-M3 may correspond

to substructures identified in the cluster A2142 by Owers et al. (2011), as discussed also in Einasto et al. (2018), and recently in Liu et al. (2018). We refer to these papers for details about substructures in the cluster A2142. In Fig. A.1 we show the distribution of Gr5 galaxies together with galaxies from A2142 cluster and its infalling subclusters and group (M1 - M3, and C3) in the sky plane and in the sky-velocity plane. This figure shows that the group Gr5 lies as close to the main cluster as its infalling subclusters. Galaxy populations in Gr5 are very similar to those in an infalling subcluster M1 embedding galaxies with old, passive stellar populations (Einasto et al. 2018), with median values of the $D_n(4000)$ index 1.8 (Gr5), and 1.9 (M1). The group G5 and subcluster M1 may be parts of a small infalling filament.

Group Gr3 is the richest galaxy group in the supercluster main body with 54 member galaxies near the cluster A2142 at median clustercentric distance of $3.3 h^{-1}$ Mpc. The analysis of the structure of Gr3 with *Mclust*, using as input sky coordinates and velocities of its member galaxies, showed that the group consists of three components. Such model has the highest value of BIC among all models considered by *mclust*. In this case the mean uncertainty of galaxies to belong to components was less than 10^{-4} . One-component model is not favoured by *mclust*. According to BIC values, the best such model (with the highest BIC value of the one-component models) is in 17th place among all models.

We present the PPS diagram of Gr3 galaxies in three components in Fig. A.2. In both figures galaxies with old stellar populations (divided using $D_n(4000)$ index) are plotted with red symbols and galaxies with young stellar populations with blue symbols.

The first component of Gr3, C1, has 26 galaxies. Figure A.2 shows that within the projected distance from the group centre at the brightest group galaxy (BGG1) up to $D_{gr} \approx 0.5 h^{-1}$ Mpc all galaxies (with one exception) in the group have old stellar populations with ages over 8 Gyr. They are almost all at the same redshift, with the velocity differences less than 250 km s^{-1} . The brightest galaxy in this group is FR II radio galaxy. Most galaxies with young stellar populations lie at distances $D_{gr} > 1.0 h^{-1}$ Mpc from the brightest galaxy. The radio lobes of this galaxy are aligned with the supercluster axis.

The second component of Gr3, C2 with 19 galaxies lies along the supercluster axis with position angle of $73 \pm 5^\circ$. Figure A.2 shows that galaxies in this component have positive velocities in respect of the main component of the group. They may not lie in the infall zone of C1.

Galaxies from the third component C3 with nine member galaxies have negative velocities in respect of the first component, and they lie in the infall zone of C1. The component C3 embeds one luminous galaxy with very old stellar populations (with ages over 8 Gyr) only, resembling typical poor galaxy group with bright main galaxy and fainter satellites.

The difference in galaxy velocities supports the possibility that C2 is a small separate group on the supercluster axis. It is combined together with the first component because of high density of galaxies and groups in the supercluster core where the criteria to define galaxy groups used in Tempel et al. (2014b) may join different groups. Small magnitude gap between the luminosities of the brightest galaxies in the group shows that the group is still forming.

Bird et al. (2008) shows that redder galaxies have an increased probability of embedding radio sources, and the radio fraction increases with the luminosity of host galaxy. This may be why the brightest galaxy in a group is FR II radio galaxy.

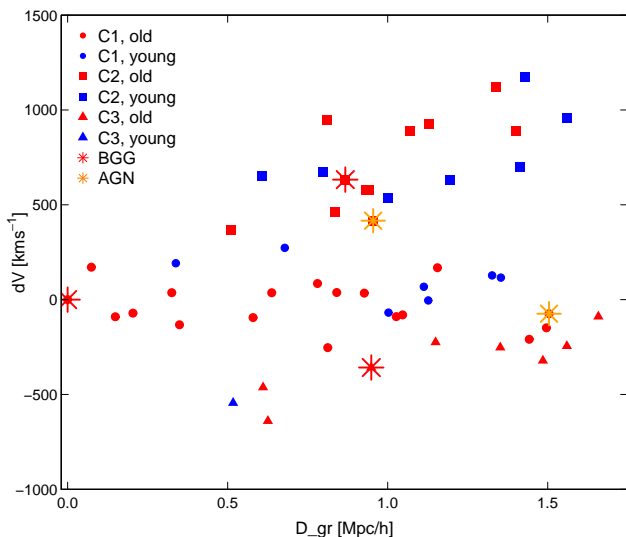


Fig. A.2. Velocity of galaxies with respect to the group mean velocity vs. the projected distance from the group centre D_{gr} at the brightest galaxy of the first component in Gr3 (BGG1) for the components of the group Gr3. Red symbols show galaxies with old stellar populations ($D_n(4000) \geq 1.55$), and blue symbols denote galaxies with young stellar populations ($D_n(4000) < 1.55$). Filled circles denote galaxies from the component C1, squares from component C2, and triangles from component C3. Red stars show the location of the BGG of each component, and orange stars correspond to AGNs.

Group Gr4 is a group of 11 galaxies with very elongated shape on the supercluster axis. Gr4 is aligned along the supercluster axis with position angle of $54 \pm 7^\circ$. The brightest galaxy of this group lies in the centre of the group, this is one of AGNs in the supercluster, and faint radio source according to VLA FIRST survey data at 1.4 GHz. Its low flux level (19.5 mJy) suggests that the radio emission most likely comes from star formation processes. The brightest galaxy in the group is also aligned along the supercluster axis. In this group all galaxies closer to the main cluster than the brightest galaxy have old stellar populations. All galaxies with young stellar populations lie farther away from the central cluster. We may suppose that the shape and orientation of the group and its BGG, as well as the stellar populations of galaxies in the group are affected by the infall into the main cluster.

Groups Gr6 and Gr7 lie close together along the supercluster axis at clustercentric distances of $7 h^{-1}$ Mpc and $6 h^{-1}$ Mpc, correspondingly, out of the collapsing core of the supercluster. The Gr7 embeds one of the AGNs in the supercluster, which is also a faint radio source. It also has one recently quenched galaxy, located near virial radius of the group. The Gr7 group hosts three galaxies with very old stellar populations having ages $t > 9.5$ Gyr, while Gr6 has seven galaxies with such old stellar populations, and no AGNs and recently quenched galaxies. The supercluster axis is probably the preferred direction of galaxy and group infall into the main cluster (Venturi et al. 2017; Einasto et al. 2018). On this axis Gr7 is closer to the main cluster than Gr6, and AGN phenomenon and stellar populations of galaxies in this group may be affected by this.

Groups Gr1 and Gr9 are groups of 27 and 21 galaxies, respectively. They are located away from the supercluster axis, at the clustercentric distance of $4.4 h^{-1}$ Mpc and $5.4 h^{-1}$ Mpc. In the PPS diagram (Fig. 6) galaxies from Gr1 have the highest positive values of their velocities in respect of the cluster centre. In Gr9 the third brightest galaxy is an AGN. Both Gr1 and Gr9 host one

recently quenched galaxy. Galaxies in these groups have younger stellar populations that any group in the supercluster main body at the supercluster axis, having median ages $t < 4$ Gyr.

Group Gr8 is a rich group with 32 member galaxies on the supercluster axis at the distance of almost $10 h^{-1}$ Mpc from the supercluster centre. It is aligned along the supercluster axis, with position angle of $55 \pm 13^\circ$. In Fig. A.3 we plot the PPS diagram for this group, together with neighbouring group of 11 galaxies, Gr10. Figure A.3 suggests that 80% of galaxies in Gr8 have negative velocity offsets in respect of the main galaxy of Gr8. These galaxies may be recently accreted into the cluster, or still infalling (we refer to Sect. 3.1 about the possible interpretation of the PPS diagram, and also to Fig. 13 in Haines et al. 2015). It is also possible that the brightest galaxy in this group has positive velocity offset in respect to the group centre.

Galaxies from Gr10 have negative velocity offsets with respect to the main galaxy of Gr8, so that they lie in the infall zone of Gr8, at distances approximately $2 - 3 h^{-1}$ Mpc from the Gr8 brightest galaxy. This can be interpreted so that group Gr10 is falling into the Gr8 along the supercluster axis (see also the sky distribution of galaxies in these groups in Figs. 1 and 4). The radius of a collapsing region around Gr8 is $R_T \approx 3.3 h^{-1}$ Mpc (Sect. 6.2), thus galaxies from Gr10 are embedded in this region. It is also possible that Gr8 and Gr10 already form a single group, elongated along the supercluster axis, and this group is split into separate systems by our group finding algorithm. Figure A.3 shows that the central part of the group up to its virial radius, $\approx 0.5 h^{-1}$ Mpc is populated with galaxies with old stellar populations. Six out of nine star-forming galaxies with young stellar populations in groups Gr8 and Gr10, and recently quenched galaxies lie in the the projected distance interval from the group centre approximately $1 - 2.5 h^{-1}$ Mpc, where groups may merge. It is possible that star formation in these galaxies is triggered by group merger.

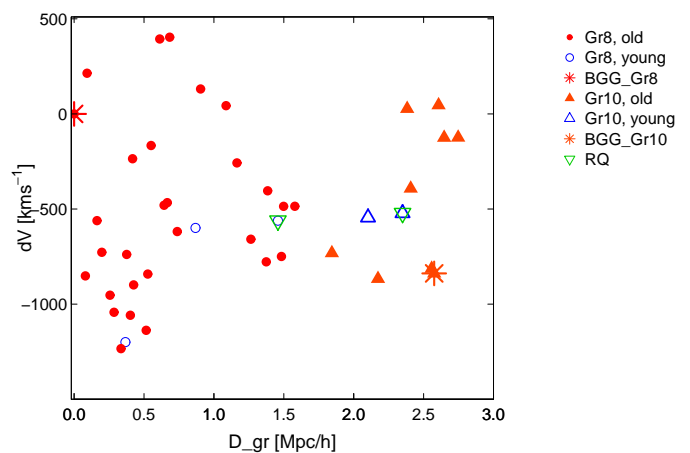


Fig. A.3. Velocity of galaxies with respect to the cluster mean velocity vs. the projected distance from the group Gr8 centre D_{gr} for the galaxies from Gr8 with Gr10. Filled red symbols show galaxies with old stellar populations ($D_n(4000) \geq 1.55$), and empty blue symbols denote galaxies with young stellar populations ($D_n(4000) < 1.55$). Green triangles indicate recently quenched galaxies (see text for definition). Red stars show the location of the BGGs.

The group Gr12 with 19 member galaxies (possibly up to 25, if we include galaxies omitted because of fibre collisions) in the supercluster tail hosts two AGNs and even three recently quenched galaxies. This is the largest number of recently quenched galaxies among rich groups in the supercluster. This group hosts the lowest percentage of old, passive galaxies among

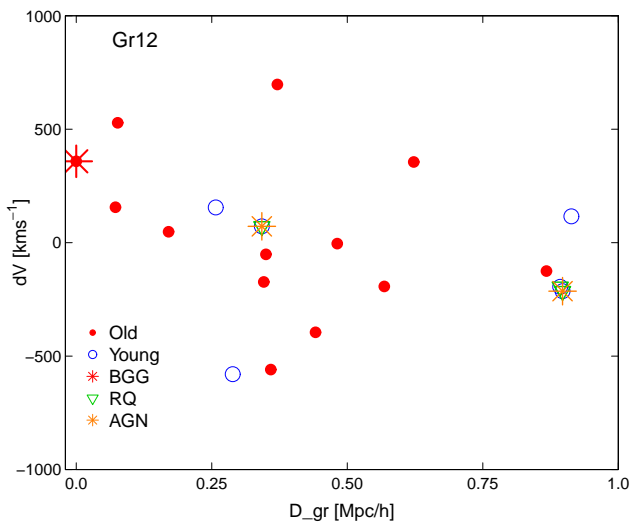


Fig. A.4. Velocity of galaxies with respect to the cluster mean velocity vs. the projected distance from the group centre D_{gr} for group Gr12 galaxies. Filled red symbols show galaxies with old stellar populations ($D_n(4000) \geq 1.55$), and empty blue symbols denote galaxies with young stellar populations ($D_n(4000) < 1.55$). Green triangles indicate recently quenched galaxies, and orange stars denote AGNs. Red star shows the location of the BGG.

groups on the supercluster axis. In Fig. A.4 we plot the PPS diagram for galaxies in this group. It shows that galaxies with old stellar populations, AGNs, and recently quenched galaxies lie at the projected distance from the group centre D_{gr} larger than $0.25 h^{-1} \text{Mpc}$, which is close to the virial radius of the group, and at the borders of the group.

Groups Gr13 and Gr14 lie at the edge of the supercluster. In Fig. A.5 we present the PPS diagram of groups Gr13 and Gr14. This figure shows that galaxies from both groups lie at overlapping regions of the PPS diagram suggesting that these groups are merging. This agrees with the prediction of the spherical collapse model which tells that the mass of these groups is enough to become a collapsed system (Einasto et al. 2015). Gr13 and Gr14 may already form a single group, which is split into separate systems by our group finding algorithm. At the projected distances from the group centre D_{gr} up to $0.5 h^{-1} \text{Mpc}$ (approximately the virial radius of the group) all galaxies in Gr13 have old stellar populations. Almost all galaxies that have young stellar populations lie in the overlapping region of the two galaxy groups, at the projected distances from the group centre approximately $0.5 - 1.0 h^{-1} \text{Mpc}$. Here lie also recently quenched galaxies and AGNs. In Gr14 the median age of stellar populations of galaxies is the lowest among groups in SCI 2142. Star formation, ages of stellar populations, and recent quenching in these galaxies may be triggered by group merger, which could also trigger the activity of AGNs.

Appendix B: Spherical collapse model

The spherical collapse model describes the evolution of a spherical perturbation in an expanding universe. This model was studied, for example, by Peebles (1980), Peebles (1984), and Lahav et al. (1991). In the standard models with cosmological constant, the dark energy started accelerating the expansion at the redshift $z \approx 0.7$ and the formation of structure slowed down. At the present epoch, the largest bound structures are just forming. In the future evolution of the universe, these bound systems

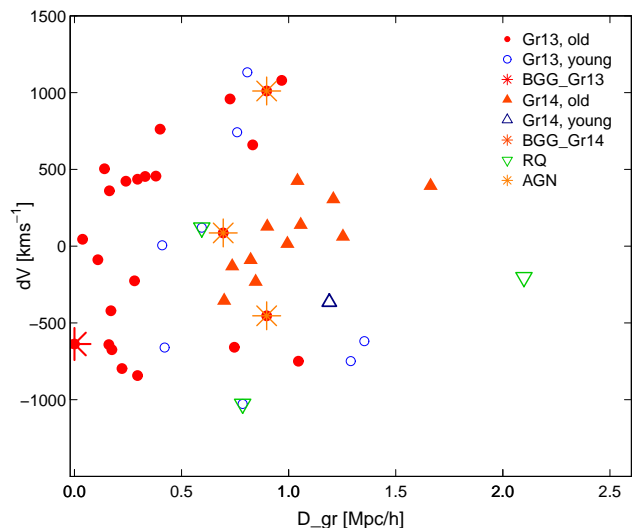


Fig. A.5. Velocity of galaxies with respect to the cluster mean velocity vs. the projected distance from the group Gr13 centre D_{gr} for the galaxies from Gr13 with Gr14. Notations as in Fig. A.4.

separate from each other at an accelerating rate, forming isolated ‘island universes’ (Chiueh & He 2002; Dünner et al. 2006).

Under the assumption of sphericity, the dynamics of a collapsing shell is determined by the mass in its interior. The evolution of a collapsing shell has several epochs which can be characterised by density contrasts (Chon et al. 2015; Gramann et al. 2015). These density contrasts can be used to derive the relations between radius of a perturbation and the interior mass for each essential epoch.

For a spherical volume the density ratio to the mean density (overdensity) $\Delta\rho = \rho/\rho_m$ can be calculated as in Einasto et al. (2016)

$$\Delta\rho = 6.88 \Omega_m^{-1} \left(\frac{M}{10^{15} h^{-1} M_\odot} \right) \left(\frac{R}{5 h^{-1} \text{Mpc}} \right)^{-3}. \quad (\text{B.1})$$

From Eq. (B.1) we can find the mass of a structure as

$$M(R) = 1.45 \cdot 10^{14} \Omega_m \Delta\rho (R/5 h^{-1} \text{Mpc})^3 h^{-1} M_\odot. \quad (\text{B.2})$$

Turnaround. One essential moment in the evolution of a spherical perturbation is called turnaround, the moment when the sphere stops expanding together with the universe and the collapse begins. At the turnaround, the perturbation decouples entirely from the Hubble flow of the homogeneous background. The spherically averaged radial velocity around a system in the shell of radius R can be written as $u = HR - v_{\text{pec}}$, where $v_H = HR$ is the Hubble expansion velocity and v_{pec} is the averaged radial peculiar velocity towards the centre of the system. At the turnaround, the peculiar velocity $v_{\text{pec}} = HR$ and $u = 0$.

The peculiar velocity v_{pec} is directly related to the overdensity $\Delta\rho$. In the model with a critical mass density, the overdensity at the turnaround is $\Delta\rho_T = 5.55$ and it does not change with time. In the standard models with cosmological constant, the characteristic density contrasts increase during the evolution. For $\Omega_m = 0.27$ and $\Omega_\Lambda = 0.73$ the overdensity at the turnaround at redshift $z = 0$ is $\Delta\rho_T = 13.1$ and the mass of a structure at the turnaround is (Gramann et al. 2015)

$$M_T(R) = 5.1 \cdot 10^{14} (R/5 h^{-1} \text{Mpc})^3 h^{-1} M_\odot. \quad (\text{B.3})$$

At the redshift $z = 0.5$, the overdensity at the turnaround in the spherical collapse model is $\Delta\rho_T = 8.0$ and the mass of a structure at the turnaround is

$$M_T(R) = 3.1 \cdot 10^{14} \left(R/5h^{-1}\text{Mpc} \right)^3 h^{-1} M_\odot. \quad (\text{B.4})$$

At the redshift $z = 1.0$, the overdensity at the turnaround is $\Delta\rho_T = 6.6$.

Future collapse. The superclusters that have not reached the turnaround at present may eventually turnaround and collapse in the future (Dünner et al. 2006). Chon et al. (2015) showed that for $\Omega_m = 0.27$ the overdensity for the future collapse $\Delta\rho_{\text{FC}} = 8.73$, which gives the minimum mass of the structure that will turn around and collapse in the future as

$$M_{\text{FC}}(R) = 3.4 \cdot 10^{14} \left(R/5h^{-1}\text{Mpc} \right)^3 h^{-1} M_\odot. \quad (\text{B.5})$$

Figure B.1 shows the overdensities for the turnaround and future collapse from redshift $z = 1.0$ to the present, $z = 0.0$, in the standard model with $\Omega_m = 0.27$ and $\Omega_\Lambda = 0.73$, in the model with $\Omega_m = 0.3$ and $\Omega_\Lambda = 0.7$, and in the model with a critical mass density. In this model the overdensity at the turnaround is $\Delta\rho_T = 5.55$ and it does not change with time.

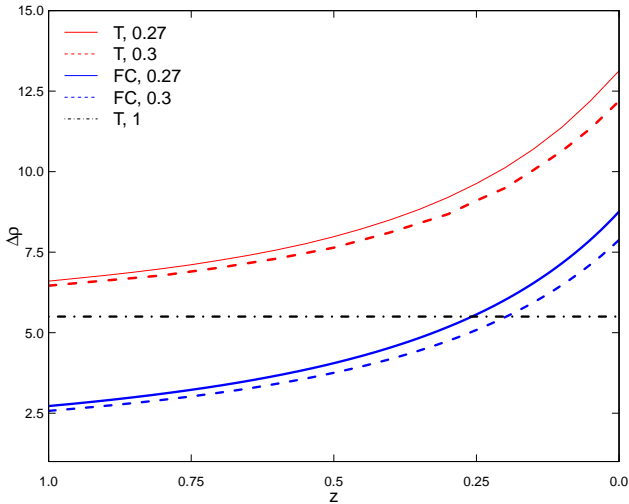


Fig. B.1. Evolution of characteristic density contrasts for the turnaround and future collapse with redshift z . The solid lines correspond to $\Omega_m = 0.27$ and dashed lines to $\Omega_m = 0.3$. Red lines show turnaround, and blue lines show future collapse. The dot-dashed line corresponds to the universe with a critical mass density.